

**Effect of Holmium Substitution on Structural, Electrical, and Magnetic
Properties of Manganese-Zinc Ferrites**

Nil Rani Kundu



Department of Physics
BANGLADESH UNIVERSITY OF ENGINEERING AND TECHNOLOGY

**Effect of Holmium Substitution on Structural, Electrical, and Magnetic
Properties of Manganese-Zinc Ferrites**

by

Nila Rani Kundu

Roll No : 1014143015P

Session : October 2014

MASTER OF PHILOSOPHY IN PHYSICS






Department of Physics

BANGLADESH UNIVERSITY OF ENGINEERING AND TECHNOLOGY

March 2021

The thesis titled “Effect of Holmium Substitution on Structural, Electrical, and Magnetic Properties of Manganese-Zinc Ferrites” submitted by Nila Rani Kundu, Roll No.: 1014143015P, Session: October-2014, has been accepted as satisfactory in partial fulfillment of the requirement for the degree of Master of Philosophy (M. Phil.) in Physics on 27 March, 2021.

BOARD OF EXAMINERS

1. 
(_____)
Chairman
Dr. A. K. M. Akther Hossain (Supervisor)
Professor, Department of Physics, BUET, Dhaka.
2. 
(_____)
Member
(Ex-Officio)
Dr. Md. Rafi Uddin
Professor and Head, Department of Physics,
BUET, Dhaka-1000.
3. 
(_____)
Member
Dr. Md. Feroz Alam Khan
Professor, Department of Physics, BUET,
Dhaka-1000.
4. 
(_____)
Member
Dr. Muhammed Samir Ullah
Associate Professor, Department of Physics, BUET,
Dhaka-1000.
5. 
(_____)
(External)
Member
Dr. Mohammed Nazrul Islam Khan
Chief Scientific Officer, Material Science Division
Atomic Energy Centre, Dhaka-1000.

CANDIDATE'S DECLARATION

It is hereby declared that this thesis or any part of it has not been submitted elsewhere for the award of any degree or diploma.

Nila Rani Kundu

*Dedicated To
My
Beloved Family*

Acknowledgements

During the course of this thesis work, I have been accompanied and supported by many people. It is the pleasant moment and opportunity for me to express my gratitude for all of them. First of all I express all my admiration and devotion to the God, the most beneficent who has enabled me to perform this research work and to submit this thesis.

I express my sincere thanks to my honorable supervisor Prof. Dr. A. K. M. Akther Hossain, Department of Physics, Bangladesh University of Engineering and Technology (BUET), for his support and scientific attitude have meant a great deal to me. His constant striving for excellence coupled with his quest for knowledge will always remain a source of inspiration for me. I am deeply indebted to him for his immense help, suggestions and the inspiring discussions during writing and completion of this thesis.

I am very grateful to Dr. Md. Rafi Uddin, Professor & Head, Department of Physics, BUET, Dhaka, Bangladesh for his valuable suggestions and inspiration.

I would like to acknowledge all my teachers, Prof. Dr. Md. Abu Hashan Bhuiyan, Prof. Dr. Jiban Podder, Prof. Dr. Md. Feroz Alam Khan, Mrs. Fahim Khanam, Prof. Dr. Md. Mostak Hossain, Prof. Dr. Afia Begum, Prof. Dr. Forhad Mina, Prof. Dr. Nasreen Akter, Prof. Dr. Mohammed Abdul Basith, Dr. Muhammad Samir Ullah for their cooperation. And special thanks go to Material Science Division, Atomic Energy Centre, Dhaka (AECD) for allowing me to use laboratory facility during my research work.

I am so thankful to all members of the Solid State Physics Research Laboratory and Department of Glass & Ceramic Engineering (GCE), BUET for their cooperation and constant support throughout the research. I would like to extend my gratitude to all of my friends, youngers, relatives and others colleagues for their good wishes and cooperation throughout the study.

Finally, I would mention a very special gratefulness for the moral support and sustaining inspiration provided by the members of my family (specially my husband). This dissertation would never have been possible without their love and affection.

(Nila Rani Kundu)

Author

ABSTRACT

Influence of Ho^{3+} substitution on the structural, magnetic and dielectric properties of various $\text{Mn}_{0.55}\text{Zn}_{0.45}\text{Ho}_x\text{Fe}_{2-x}\text{O}_4$ are thoroughly investigated. X-ray diffraction patterns indicated that the samples possess fairly single-phase cubic spinel structure for a small amount of Ho^{3+} substitution. The value of lattice parameter increases with increasing Ho^{3+} content. The bulk density decreases and porosity increases with increasing Ho^{3+} content. FESEM images showed that Ho^{3+} have a significant effect on the grain growth. The maximum value of real part of initial permeability (338) is obtained for $x=0.03$ sample. Due to the addition of Ho^{3+} there is a decrease of saturation magnetization from 71 to 44 emu/g and increase of the coercivity from 21 to 70 Oe. It was observed that real part of the dielectric constant decrease with increasing of frequency on the basis of Wagner and Koop's theory. The mechanism of conduction may be explained by the small polaron hopping model.

CONTENTS

Acknowledgements	V
Abstract	VI
Contents	VII
List of Figures	X
List of Tables	XII
List of Symbols and Abbreviations	XIII

1. INTRODUCTION

1.1 Introduction	1
1.2 Motivation of the Present Research	2
1.3 Objectives	4
1.3 Outline of the Thesis	5

2. LITERATURE REVIEW AND THEORETICAL ASPECTS

2.1 Review of Earlier Works	6
-----------------------------	---

3. MATERIALS AND METHODS

3.1 Sample Preparation	16
3.2 Standard Solid State Reaction Technique	17
3.2.1 Reagents	17
3.2.2 Mixing	17
3.2.3 Calcination	18
3.2.4 Green body preparation	19
3.2.5 Uniaxial pressing	20
3.2.6 Sintering	21
3.2.7 Etching	22
3.3 Preparation of the present samples	22
3.4 Structural and Morphological Characterization	24

3.4.1 X-ray diffraction	24
3.4.2 Density and porosity calculation	25
3.4.3 Study of microstructure	26
3.4.4 Energy-dispersive X-ray spectroscopy	28
3.5 Complex Initial Permeability Measurement	28
3.5.1 Techniques for the initial permeability measurement	29
3.5.2 Frequency dependent characteristics	29
3.6 DC Magnetization Measurement Technique	30
3.7 Dielectric Measurement Techniques	31
3.7.1 Measurement of ac-conductivity	32
3.7.2 Impedance spectroscopy	33
3.7.3 Modulus spectra	35

4. RESULTS AND DISCUSSION

4.1 Samples Sintering Temperature and Density	36
4.2 X-ray Diffraction Analysis	37
4.3 Lattice Parameters	38
4.4 Porosity	39
4.5 Microstructural Analysis	40
4.6 Energy Dispersive Spectroscopy Analysis	41
4.7 Magnetic Properties	44
4.7.1 Complex initial permeability	44
4.7.2 Loss factor	48
4.7.3 Relative quality factor	50
4.7.4 Hysteresis loop analysis	51
4.8 Dielectric Properties	52
4.8.1 Dielectric constant	52
4.8.2 Dielectric loss factor	54
4.8.3 The ac-Conductivity	55
4.8.4 Complex impedance spectra analysis	57

5. CONCLUSIONS

5.1 Conclusions 63

5.2 Suggestions for Future Work 65

References 67

Appendix 79

List of Figures

Fig. 2.1	X-ray diffraction patterns of $\text{Mn}_{0.5}\text{Zn}_{0.5}\text{R}_{0.05}\text{Fe}_{1.95}\text{O}_4$, where R = Tb, Ce, La, Th.	6
Fig. 2.2	a. Frequency dependence of initial permeability (μ_i) & b. Frequency dependence of quality factor (Q).	7
Fig. 2.3	Dielectric constant with frequency of $\text{Mn}_{0.5}\text{Zn}_{0.5}\text{Sc}_y\text{Fe}_{2-y}\text{O}_4$.	8
Fig. 2.4	Room temperature $M-H$ curves for $\text{Mn}_{0.5}\text{Zn}_{0.5}\text{La}_x\text{Fe}_{2-x}\text{O}_4$.	9
Fig. 2.5	XRD patterns for as-synthesized $\text{Mn}_{0.4}\text{Zn}_{0.6}\text{Sm}_{0.04}\text{Gd}_{0.04}\text{Fe}_{1.92}\text{O}_4$.	10
Fig. 2.6	Magnetic hysteresis loop for $\text{Mn}_{0.4}\text{Zn}_{0.6}\text{Sm}_x\text{Gd}_y\text{Fe}_{2-(x+y)}\text{O}_4$ samples.	10
Fig. 2.7	XRD Patterns of $\text{Li}_{1.2}\text{Zn}_{0.4}\text{Ho}_x\text{Fe}_{2-x}\text{O}_4$.	11
Fig. 2.8	SEM images of $\text{Ho}_x\text{CoFe}_{2x}\text{O}_4$.	12
Fig. 2.9	Room temperature $M-H$ curves for $\text{Ni}_{0.7}\text{Zn}_{0.3}\text{Ho}_{2x}\text{Fe}_{2-2x}\text{O}_4$.	13
Fig. 2.10	Frequency dependent resistivity of $\text{CoFe}_{2-x}\text{Ho}_x\text{O}_4$ samples.	13
Fig. 2.11	Variations of ϵ' with $\ln f$ of $\text{NiHo}_x\text{Fe}_{2x}\text{O}_4$.	14
Fig. 2.12	Variations of $\tan\delta$ with $\ln f$ of $\text{NiHo}_x\text{Fe}_{2x}\text{O}_4$.	14
Fig. 2.13	(a) The frequency dependence of real part of electric modulus M' of $\text{Li}_{1.2}\text{Co}_{0.4}\text{Ho}_x\text{Fe}_{2-x}\text{O}_4$ and (b) The frequency dependence of the imaginary part of the electric modulus M'' of $\text{Li}_{1.2}\text{Co}_{0.4}\text{Ho}_x\text{Fe}_{2-x}\text{O}_4$.	15
Fig. 3.1	Balance, mortar, and pestle	18
Fig. 3.2	Typical diagram of a crucible and a programmable electric furnace.	19
Fig. 3.3	Schematic diagram of uniaxial pressing technique.	20
Fig. 3.4	Schematic representation of sintering stages: (a) greenbody, (b) initial stage, (c) intermediate stage, and (d) final stage.	21
Fig. 3.5	Graphical representation for the synthesis of ceramics samples by the solid-state reaction route.	23
Fig. 3.6	(a) Disk- and, (b) toroid- shaped samples.	24
Fig. 3.7	Bragg law of X-ray diffraction.	25
Fig. 3.8	Various types of signals which are generated by SEM.	27
Fig. 3.9	FESEM setup.	28
Fig. 3.10	Toroid shaped sample for the measurement of permeability.	29
Fig. 3.11	Silver paste painted two probe arrangements on the sintered sample.	32
Fig. 3.12	The impedance plot for a circuit of a resistor and a capacitor in parallel and (b) the corresponding equivalent circuit.	34
Fig. 3.13	The impedance plot for an ideal polycrystalline sample and (b) the corresponding equivalent circuit.	34

Fig. 4.1	Variation of ρ_B with Ho^{3+} contents of various $\text{Mn}_{0.55}\text{Zn}_{0.45}\text{Ho}_x\text{Fe}_{2-x}\text{O}_4$ for various T_s .	36
Fig. 4.2	XRD patterns of various $\text{Mn}_{0.55}\text{Zn}_{0.45}\text{Ho}_x\text{Fe}_{2-x}\text{O}_4$.	37
Fig. 4.3	Variation of a_0 with Ho^{3+} content of various $\text{Mn}_{0.55}\text{Zn}_{0.45}\text{Ho}_x\text{Fe}_{2-x}\text{O}_4$.	38
Fig. 4.4	Variation of ρ_{th} , ρ_B , and P with Ho^{3+} content of various $\text{Mn}_{0.55}\text{Zn}_{0.45}\text{Ho}_x\text{Fe}_{2-x}\text{O}_4$ sintered at 1225°C .	39
Fig. 4.5	The microstructure of various $\text{Mn}_{0.55}\text{Zn}_{0.45}\text{Ho}_x\text{Fe}_{2-x}\text{O}_4$ samples sintered at 1225°C .	40
Fig. 4.6	FESEM images along with EDS spectrum of $x=0.00$, $x=0.03$, $x=0.06$, $x=0.09$, and $x=0.12$ samples of $\text{Mn}_{0.55}\text{Zn}_{0.45}\text{Ho}_x\text{Fe}_{2-x}\text{O}_4$ sintered at 1225°C .	44
Fig. 4.7	The μ_i' spectra for various $\text{Mn}_{0.55}\text{Zn}_{0.45}\text{Ho}_x\text{Fe}_{2-x}\text{O}_4$ sintered at different T_s .	46
Fig. 4.8	The variation of μ_i' (a) at 1 kHz, (b) at 10 kHz, and (c) at 1 MHz with Ho^{3+} content for $\text{Mn}_{0.55}\text{Zn}_{0.45}\text{Ho}_x\text{Fe}_{2-x}\text{O}_4$ sintered at different T_s .	47
Fig. 4.9	Variation of $\tan\delta_M$ with frequency for $\text{Mn}_{0.55}\text{Zn}_{0.45}\text{Ho}_x\text{Fe}_{2-x}\text{O}_4$ sintered at different T_s .	49
Fig. 4.10	Variation of RQF with frequency for $\text{Mn}_{0.55}\text{Zn}_{0.45}\text{Ho}_x\text{Fe}_{2-x}\text{O}_4$ sintered at different T_s .	50
Fig. 4.11	M - H curves for various $\text{Mn}_{0.55}\text{Zn}_{0.45}\text{Ho}_x\text{Fe}_{2-x}\text{O}_4$.	52
Fig. 4.12	Variation of ϵ' with frequency for $\text{Mn}_{0.55}\text{Zn}_{0.45}\text{Ho}_x\text{Fe}_{2-x}\text{O}_4$ sintered at different T_s .	53
Fig. 4.13	Variation of $\tan\delta_E$ with frequency for $\text{Mn}_{0.55}\text{Zn}_{0.45}\text{Ho}_x\text{Fe}_{2-x}\text{O}_4$ sintered at different T_s .	54
Fig. 4.14	Variation of ζ_{ac} with frequency for $\text{Mn}_{0.55}\text{Zn}_{0.45}\text{Ho}_x\text{Fe}_{2-x}\text{O}_4$ sintered at different T_s .	56
Fig. 4.15	Variation of $\log\zeta_{ac}$ with $\log\omega$ for $\text{Mn}_{0.55}\text{Zn}_{0.45}\text{Ho}_x\text{Fe}_{2-x}\text{O}_4$ sintered at different T_s .	57
Fig. 4.16	Variation of (a) Z' and (b) Z'' with frequency for $\text{Mn}_{0.55}\text{Zn}_{0.45}\text{Ho}_x\text{Fe}_{2-x}\text{O}_4$ sintered at different T_s .	58
Fig. 4.17	Variation of (a) M' and (b) M'' with frequency for $\text{Mn}_{0.55}\text{Zn}_{0.45}\text{Ho}_x\text{Fe}_{2-x}\text{O}_4$ sintered at different T_s .	59
Fig. 4.18	(a). The Cole-Cole plot of $\text{Mn}_{0.55}\text{Zn}_{0.45}\text{Ho}_x\text{Fe}_{2-x}\text{O}_4$. (b) Equivalent circuit model.	61

List of Tables

	Pages
4.1. Data of ρ_{th} , ρ_B and P of various $Mn_{0.55}Zn_{0.45}Ho_xFe_{2-x}O_4$ Samples.	39
4.2. Data of M_s , H_c , M_r , n_B , and K_u of various $Mn_{0.55}Zn_{0.45}Ho_xFe_{2-x}O_4$ Samples.	51

List of Symbols and Abbreviations

μ_B	Bohr Megneton
m_s	Spin quantum number
B	Flux density
H	Magnetic field
$F(\theta)$	Nelson-Riley function
f_r	Resonance frequency
g	Landé splitting factor
χ	Magnetic susceptibility
J	Exchange integral
H_r	Coercivity
L_s	Self-inductance of the sample core
L_o	Inductance of the winding coil without sample
M	Magnetization
M_s	Saturation magnetization
N_A	Avogadro's number
P	Porosity
ρ_{th}	Theoretical Density
ρ_B	Bulk Density
a_0	Lattice parameter
Q	Relative quality factor
T_c	Curie temperature
C	Curie constant
T_s	Sintering temperature
$\tan\delta$	Loss factor
Z	Complex impedance
α	Restoring force coefficient
β	Viscous damping factor
γ	Domain wall energy
ω	Angular velocity
δ_w	Domain wall thickness
μ_i	Initial permeability
μ'	Real part of complex permeability
μ''	Imaginary part of complex permeability
ε	Dielectric constant
χ_{spin}	Intrinsic rotational susceptibility
χ_w	Domain wall susceptibility
	Average Grain size

1. INTRODUCTION

1.1 Introduction

During the last few decades, spinel ferrites have been investigated for their useful applications in information storage systems, sensors, actuators, magnetic fluid, microwave absorbers and medical diagnostics. Thus much attention has been focused on the preparation and characterization of spinel ferrites [1-2]. The spinel ferrites are semi conducting in nature. The electrical and magnetic of ferrites depend on several factors including the method of preparation, sintering temperature, sintering atmosphere, chemical composition and microstructure [3-7]. It is very important that the understanding of mechanism involved changes in properties caused by addition of substitutions and provides information for the preparation of ferrites suitable for specific applications. The information regarding the crystal structure provides excellent opportunities for understanding the chemical managements of the super paramagnetic properties of spinel ferrites [8-10]. Spinel is the name of naturally occurring mineral with chemical formula MFe_2O_4 (where $M = Mn, Fe, Co, Ni, Cu,$ and Zn). The spinel structure is formed by close packed fcc array of anions with interstitial sites occupied by metal cations [11]. According to their crystal structure spinel-type ferrites are natural superlattices. It has tetrahedral A-site and octahedral B-site in AB_2O_4 crystal structure. The metal cations in both sites are distributed based on their affinity to occupy the positions which in turn are significantly dependent on the stabilization energy, ionic radii of metal cations, size of interstitial site, synthesis technique, and their synthesis reaction conditions. Ferrites are high resistive magnetic ceramics of great importance in the production of electronic components, since they reduce energy loss caused by eddy current. Their applications ranges from simple device such as small permanent magnet to sophisticated devices for the electronic industry like magnetic media used in computers, magnetic switches, magnetic cards etc [12]. These ferrites show various magnetic properties based on their chemical composition and cation distribution in tetrahedral- and octahedral-sites. On the other hand, for various technological applications like manufacturing of magnetic fluids or magnetic recording devices, the rare earth (RE) metal ion doped spinel ferrites are prioritized and widely used because of their magneto-electric and magneto-optical properties [13]. Besides, rare earth ions have typical relaxation characteristics, which

may alter the electrical and magnetic properties of ferrite. These changes are due to reordering of the cations among octahedral and tetrahedral sites. In recent years, substitution of rare-earth ions into the ferrites becomes interesting due to their improved structural, magnetic and electrical properties [14-17]. Substitution of Fe^{3+} by rare earth ions have been advantageous due to enhanced electrical and magnetic characteristics of spinel type ferrites due to RE–Fe interactions and magnetocrystalline anisotropy in the rare earth ions.

1.2 Motivation of the Present Research

A ferrite [18–21] is a ceramic material that is made up of iron oxide (Fe_2O_3) in large proportion mixed with metallic element such as barium (Ba), manganese (Mn), nickel (Ni), zinc (Zn) etc. in small proportions. The nature of both the iron oxide and the metal is electrically non-conducting and ferrimagnetic. Ferrimagnetic material is one that possesses unequal opposing magnetic moments which allow such materials to retain spontaneous magnetization. Ferrites are generally classified into two types: hard ferrites [22, 23] and soft ferrites [24–26]. Hard ferrites have high coercivity and such materials are difficult to magnetize. Therefore these materials are used in making permanent magnets which are used for applications in refrigerator, loudspeaker, washing machine, TV, communication systems, switch mode power supplies, dc-dc converters, microwave absorbing systems, high frequency applications, refrigerator, loudspeaker etc. [27–30]. On the other hand, soft ferrites have low coercivity as a result of which their magnetization can easily be altered. Soft ferrites are good conductors of magnetic field which has led to its wide range of applications in electronic industry such as developing transformer cores, high frequency inductors and as microwave components [31–34]. Furthermore, advantages of soft ferrites include high resistivity, low cost, time and temperature stability, low loss and high permeability [35-37]. In the class of soft ferrites, Mn-Zn ferrites are more preferred as they have high permeability [38], saturation magnetization [39], low power losses [40-41] and high magnetic induction [42]. Mn-Zn ferrites are also preferred over other ferrites due to their low cost and wide range of applications such as power applications [43-44], magnetic fluid [45], high frequency power supply [43], memory storage devices, TV sets, biomedicines [46], magnetic resonance, catalysis etc. On the

other hand, the magnetic properties can be changed by the substitution of various kinds of M^{2+} divalent cations (Co^{+2} , Mg^{+2} , Fe^{+2} , Mn^{+2}) or by introducing a relatively small amount of rare-earth ions [47]. Nowadays the rare earth oxides are becoming promising additives to improve the magnetic properties of ferrites. Many investigations have been carried out to improve the electrical and thermal conductivity, structural, spectral, dielectric and magnetic properties on rare earth substitution in ferrites because rare earth could drastically affect these properties due to having larger ionic radii [48]. Ahmed et al. [49] investigated the enhancement of the physical properties of rare-earth-substituted Mn–Zn ferrites ($Mn_{0.5}Zn_{0.5}R_{0.05}Fe_{1.95}O_4$, where R = Tb, La, Ce and Th) prepared by flash combustion method. The results found that samples have the single phase cubic spinel structure from XRD. Except for Mn–Zn ferrite (without substitution), another small peaks indicating the presence of secondary phase, which are identified by JCPDS card as orthoferrite ($RFeO_3$), is found. Peng et al. [50] have studied the magnetic and dielectric properties of Pr^{3+} doped Ni–Zn ferrites and reported a decrease in the dielectric parameters in the frequency range 1 MHz – 400 MHz due to Pr^{3+} substitution. Feng et al. [51] have reported the microstructure and magnetic properties of Ni–Zn–Cr doped with La^{3+} and found a decrease in magnetization along with increase in coercive force due to simultaneous substitution of Cr^{3+} and La^{3+} . Angari et al. [52] have also reported the influence of lanthanum ion on the magnetic properties of nickel ferrites. Influence of Y^{3+} ions on the magnetic and electric properties of nickel ferrites have been investigated by Ishaque et al. [53] and found an increase in the crystallite size and lattice parameter due to Y^{3+} substitution. Among all the rare earth ions, Ho^{3+} has the highest magnetic moment ($10.6 \mu_B$) [54] and is considered an important rare earth ion for use in other ferrite structures for use as permanent magnets and in the high frequency applications like microwave absorbing devices [55]. Doping of Ho^{3+} in the spinel structures can be used in high frequencies by increasing the resistivity and reducing the losses both dielectric and magnetic. Recently, many researchers investigated the effect of substitution of Fe^{3+} by Ho^{3+} on the structural, magnetic, and transport properties of cobalt ferrites with a view to enhance the electro-magnetic properties [56-57]. Ali et al. [58] have studied the structural and magnetic properties influenced by doping of Ho^{3+} in high coercivity cobalt ferrites. From this article, X-ray diffraction reveals that the substituted samples

show a second phase of HoFeO_3 along with the spinel phase. On the other hand, the magnetization (M_s) decreases while coercivity (H_c) increases with Ho^{3+} substitution. The decrease of saturation magnetization is attributed to the weakening of exchange interactions. The coercivity increases with increase of the Ho^{3+} concentration, which is attributed to the presence of an ultra-thin layer at the grain boundaries that impedes the domain wall motion. Karimunnesa et al. [57] investigated the effect of Fe^{3+} replacement by Ho^{3+} ions on the properties of $\text{CoFe}_{2-x}\text{Ho}_x\text{O}_4$. The results found that the electrical resistivity of a ferrite decreased by substituting a small quantity of Ho^{3+} as well as saturation magnetization was decreased for $\text{CoFe}_{2-x}\text{Ho}_x\text{O}_4$. The literature survey has confirmed that no investigation is available to check the influence of Ho^{3+} ions substitution into Mn-Zn ferrites with view to their structural, magnetic and high frequency dielectric characteristics. In the present study, a detailed investigation of Ho^{3+} substituted Mn-Zn ferrite with standard solid state technique has been carried out which results in the modifications of their properties.

1.3 Objectives

With the substitution of Ho^{3+} in Mn-Zn ferrites electrical resistivity, dielectric and magnetic properties are expected to be improved due to modified cation distribution between A- and B- sites in the AB_2O_4 spinel structure. The obtained results of these ferrites may be suitable for the manufacture of multifunctional devices (e.g. microwave devices, transducers, magnetic switches, sensors etc.).

The main objectives of the present research are as follows:

- Preparation of various $\text{Mn}_{0.55}\text{Zn}_{0.45}\text{Ho}_x\text{Fe}_{2-x}\text{O}_4$ ($x=0$ to 0.12 in the step of 0.03) samples using solid state reaction technique.
- Structural characterization was done by the X-ray diffraction (XRD). From the XRD results, lattice parameters, density and porosity of all the compositions are determined.
- Surface morphology and average grain sizes of all samples are investigated by a high resolution scanning electron microscope (SEM).

- Investigation of the complex initial permeability as a function of frequency of all the studied samples.
- Frequency and composition dependence of dielectric constant, dielectric loss and ac conductivity are studied.
- Impedance spectroscopy of all the samples was also studied.
- Investigation of DC magnetization.

1.4 Outline of the Thesis

The summary of the thesis is as follows:

- Chapter 1 of this thesis deals with the importance of ferrites and objectives of the present work.
- Chapter 2 gives a brief overview of the materials, theoretical background as well as crystal structure of the spinel type ferrites.
- Chapter 3 gives the details of the sample preparation and the description of different measurement techniques that have been used in this research work.
- Chapter 4 is devoted to the results of various investigations and explanation of results in the light of existing theories.
- Chapter 5 Conclusions drawn from the overall experimental results and discussion are presented.

3. MATERIALS AND METHODS

3.1 Sample Preparation

A common goal to all the ferrites is the formation of the spinel structure. Now a days, the majority of ferrite powders are made by the conventional ceramic process or solid state reaction technique. Most of the non-conventional processes are involved in producing the powder by a wet method. Among these methods, some are [67, 68]:

- i. Co-precipitation
- ii. Organic precursors
- iii. Sol-gel synthesis
- iv. Spray-drying
- v. Freeze-drying
- vi. Combustion synthesis
- vii. Glass crystallization

Both the mechanical and chemical methods have some advantages and disadvantages. The advantages of the mechanical methods include large-scale production of bulk ceramic powder at low cost and comparatively easy adaptability. However, in the conventional solid-state reaction method the particles are being coarse due to the high temperature and heating for long time [69]. Chemical methods are generally used to prepare fine powder with improved homogeneity and densification. The chemical precursors used in the sample preparation process can simply be refined to enhance the purity of the desired composition. It is also easy to control the stoichiometry and particle size with less processing time. However, the chemical techniques are generally complex than the conventional solid-state route and the large-scale production is sometimes difficult.

In this thesis, the most economical and comparatively simple mixed oxide process conventional solid-state reaction technique is used for preparing the different compositions of $\text{Mn}_{0.55}\text{Zn}_{0.45}\text{Ho}_x\text{Fe}_{2-x}\text{O}_4$.

3.2 Standard Solid State Reaction Technique

The solid-state reaction method is the most widely used technique for the synthesis of polycrystalline materials from a mixture of solid starting materials. It is a direct reaction technique between the starting raw materials (usually powders). At room temperature, solids do not react together. High temperature (often 800 to 1600°C) is required to take place the reaction at an appreciable rate. There are several factors on which the rate of reaction and feasibility depend including structural properties of the reactants, reaction conditions, surface area of the solids, reactivity of solids, and change of the thermodynamic free energy associated with the reaction [70, 71]. Solid-state reaction is generally slow because during the reaction process a large number of bonds break and the ions migrate through a solid unlike gas phase and solution reactions [69]. Diffusion acts as the limiting factor in solid state reaction. So by controlling the diffusion of the cations through the product layer the solid state reaction rate can be controlled. The reaction takes place more quickly with the increase of temperature and reaction does not take place until the reaction temperature reaches at least two third of the melting point of one of the reactants [69]. The basic steps involved in the solid state reaction method are discussed below.

3.2.1 Reagents

Reagents are the solid reactants which are used to prepare a solid sample. The selected raw materials are first weighed out according to the stoichiometry of the compound. In this case, the impurity and moisture content should be taken into consideration. Before weighing the reactants should be dried thoroughly.

3.2.2 Mixing

After weighing the required amount of raw materials, they are mechanically mixed and then grind to control the particle size and for making the mixture homogeneous. For this purpose milling operation is carried out which can reduce the particle size to 1-10 µm range [72]. For mixing small amount of reactants, generally an agate mortar and pestle are used as shown in Fig.3.1.



Fig. 3.1 Balance, mortar, and pestle.

For mixing small amount of reactants, generally an agate mortar and pestle are used as shown in Fig.3.1 Sometimes volatile organic liquid (acetone or alcohol) is used to make the mixture more homogeneous. During the mixing and grinding process the organic liquid volatilizes gradually and evaporates completely after 10 to 15 minutes. Ball milling process is adopted when the quantity of raw materials are much larger than 20 to 25 g. Since increase in surface area may increase the reaction rate, fine grained materials should be used.

3.2.3 Calcination

Next step is the solid state reaction between the constituents of the raw materials at suitable high temperature. This process is known as firing or calcinations. Calcination is typically a chemical reaction technique during which either complete or partial phase of the material is formed. During the calcinations process the unwanted gases and impurities are removed from the desired composition. It also helps in homogenization of the powder sample and reducing the shrinkage. Calcination causes the constituents to interact by inter diffusion of their ions and resulting in a homogeneous body. The control over the stoichiometry is necessary during the calcinations process and for it, volatile constituents should be compensated. This thermal treatment process can be carried out in the absence or limited supply of air. Calcination reactions occur at or above the thermal decomposition temperature of the constituent starting materials. This reaction takes place at temperature below the melting points of the raw materials [73]. The calcinations temperature is the temperature at which the standard Gibbs free energy for a particular calcination reaction is equal to zero [74]. The calcination temperature for a desired

composition can be selected from the thermo gravimetric analysis (TGA), differential thermal analysis (DTA) and the differential thermo gravimetric analysis (DTG). In general, the calcination of raw materials is involved with four physical processes [75].

- i. Linear expansion of the particles ($< 400\text{ }^{\circ}\text{C}$)
- ii. Solid phase reaction ($400\text{ to }750\text{ }^{\circ}\text{C}$)
- iii. Contraction of product ($750\text{ to }850\text{ }^{\circ}\text{C}$)
- iv. Grain growth ($> 850\text{ }^{\circ}\text{C}$)

A programmable furnace is typically used for the high temperature heat treatment. Crucible or boat can be used as container of sample. However, it is important to choose a suitable container material. The container material should be chemically inert to the reactants under the heating conditions used. A typical diagram of the container of sample and a programmable furnace are illustrated in Fig. 3.2.

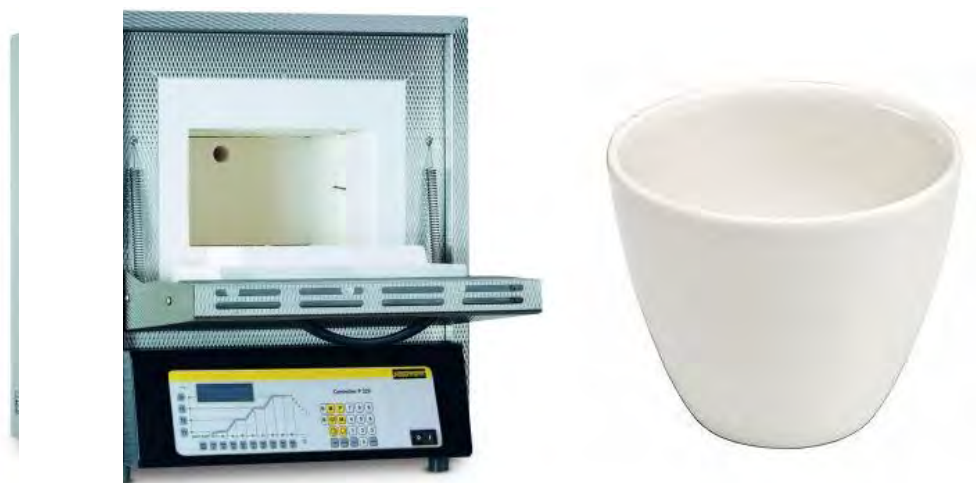


Fig. 3.2 Typical diagram of a crucible and a programmable electric furnace.

3.2.4 Green body preparation

Before further shaping the calcined powder is grind or ball milled again for few hours. Usually, the calcined powder is mixed with an organic binder (Polyvinyl alcohol- PVA) for making the sample more strengthened so that handling of the sample between the shaping and sintering process may not be difficult. It is very important that to choose such a reagent as binder which is removable from the pressed sample after sintering

without any disruptive effect. There are various methods available for shaping powder sample. These are,

- i. Uniaxial pressing
- ii. Isostatic pressing
- iii. Extrusion
- iv. Calendering
- v. Jigging
- vi. Band casting
- vii. Silk screening
- viii. Slip casting
- ix. Injection moulding

However, in the present work uniaxial pressing technique is used among these different shaping methods.

3.2.5 Uniaxial pressing

Uniaxial pressing is used to make compacts of small sizes with simple shapes of the calcined powder. It is carried out in a die having movable top. A cavity is formed at the bottom in lower portion. This cavity is filled with free flowing granulated powder and then it is struck with the top of the die. With the help of the top-punch, pressure in the range of 4000 to 8000 psi is applied by a Hydraulic press. A lot of care at various levels of mixing is needed while using this pressing technique, as samples prepared by this technique show the mechanical cracks and layering after sintering. Highly polished die and punch surfaces help to reduce wall friction and tools are made of hardened steels to minimize wear and maintain surface finish. The process is shown in Fig. 3.3.

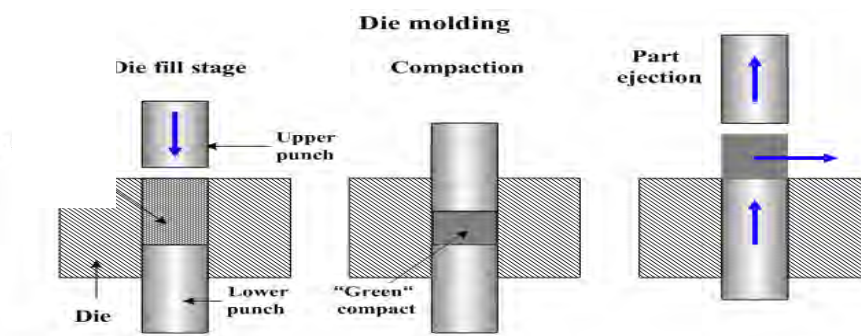


Fig. 3.3 Schematic diagram of uniaxial pressing technique [15].

3.2.6 Sintering

Sintering is the process of compacting and forming a solid mass of material by heat or pressure without melting it to the point of liquefaction. It is the process in which the green compacts are generally consolidated into strong and dense polycrystalline aggregates [69]. During sintering at an appreciable temperature, the atomic motion is more violent and the area between grains in contact increases due to the thermal expansion of the grains and finally only one interface between two grains remains. This corresponds to a state with much lower surface energy. In this state, the atoms on the grain surfaces are affected by neighboring atoms in all directions, which results in densified ceramic [73]. Sintering is effective when the process reduces the porosity and enhances properties such as strength, electrical conductivity, translucency, thermal conductivity etc.

Coble and Burke derived an empirical relationship regarding the rate of grain growth with sintering time given as follows [76],

$$= kT^n \quad (3.1)$$

where, \bar{d} stands for the mean grain diameter, n is about $\frac{1}{3}$, T is the sintering time and k is a temperature dependent parameter. Sintering can be divided into three stages as shown in Fig. 3.4.

stage-1: contact area between particles increases,

stage-2: porosity changes from open to close porosity,

stage-3: pore volume decreases and grains begin to grow.

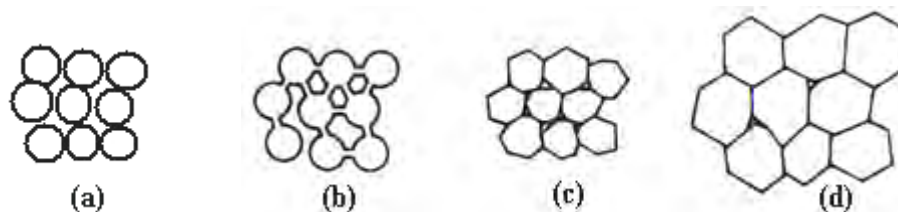


Fig. 3.4 Schematic representation of sintering stages: (a) greenbody, (b) initial stage, (c) intermediate stage, and (d) final stage [77].

In the initial stage, neighboring particles form a neck by surface diffusion and presumably also at high temperatures by an evaporation-condensation mechanism. Grain

growth begins during the intermediate stage of sintering. Since grain boundaries are the sinks for vacancies, grain growth tends to decrease the pore elimination rate due to the increase in distance between pores and grain boundaries, and by decreasing the total grain boundary surface area. In the final stage, the grain growth is considerably enhanced and the remaining pores may become isolated.

3.2.7 Etching

Etching is a technique for exposing the microscopic features of a sample. It is a process of revealing the microstructure of materials. There are several etching techniques, such as [78]-

- i. Thermal etching.
- ii. Chemical etching.
- iii. Electrolytic etching.
- iv. Plasma etching.
- v. Magnetic etching.
- vi. Molten salt etching.

In this work, thermal etching technique is used. For analyzing the microstructural features of a sample, a metallic sample must be polished to have a fine mirror like surface. However, the polished surface of a sample looks like a plain white field under a microscope. Hence, for creating a contrast between the elements of the sample's microstructure, thermal etching technique is used. In this case, the etching temperature is few hundred degrees less than that of the sample's sintering temperature. A flow chart for the synthesis of materials by the solid-state reaction route is illustrated in Fig. 3.5.

3.3 Preparation of the present samples

Various $Mn_{0.55}Zn_{0.45}Ho_xFe_{2-x}O_4$ are synthesized using the standard solid state reaction technique which is discussed in section 3.2. Powders of $MnCO_3$ (99.9%), ZnO ($\geq 99.9\%$), Ho_2O_3 (99.8%), Fe_2O_3 ($\geq 99.9\%$) were used as raw materials. Stoichiometric amounts of the raw materials are properly mixed in an agate mortar by hand milling for about 6 hours. Acetone (volatile organic liquid) is used for making the mixer more homogeneous. During the mixing and grinding process acetone gradually evaporates completely within 10 to 15 minutes.

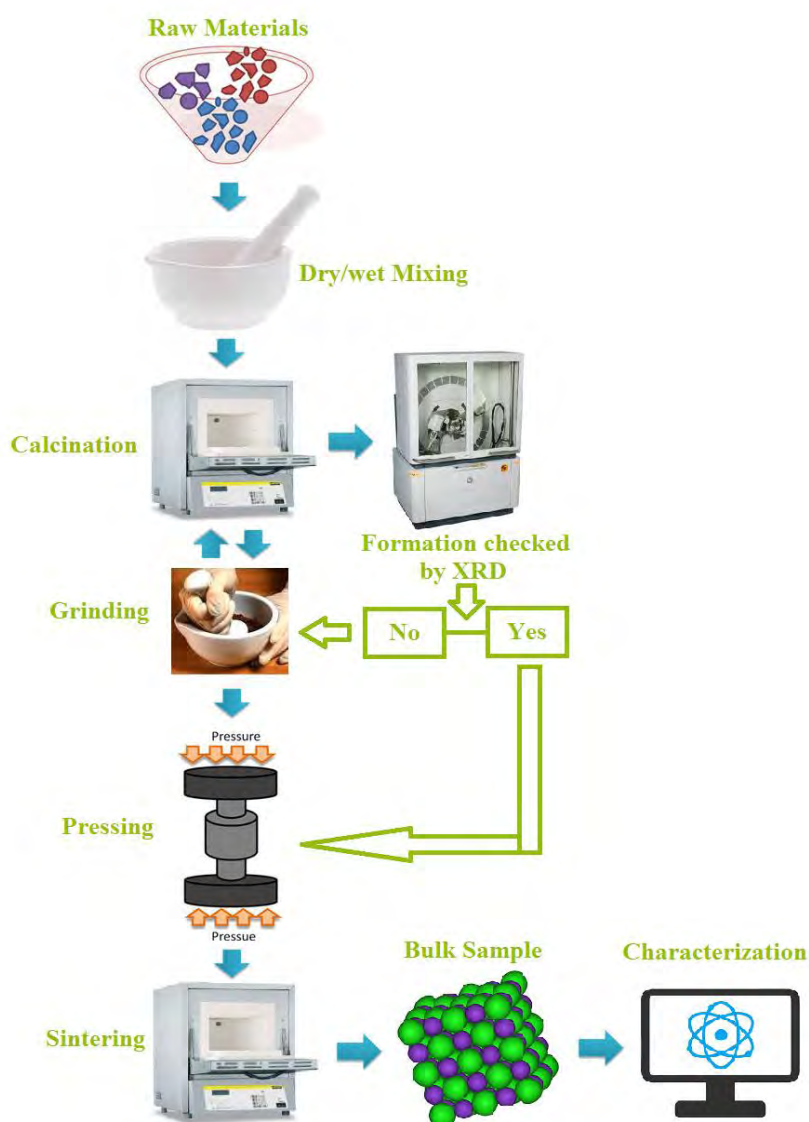


Fig. 3.5 Graphical representation for the synthesis of ceramics samples by the solid-state reaction route.

After grinding and mixing properly, the dried powders are then calcined in an alumina crucible by using a programmable electric furnace at 900°C for 5 hours in the air with heating and cooling rates of 10 and $5^{\circ}\text{C}/\text{min}$, respectively. The calcined powder is then re-milled for 4 hours for ensuring proper homogenization. Finally, the dried fine powders are used to prepare the disc- and toroid- shaped green body (diameter 13 mm and thickness 1-1.5 mm) by applying uniaxial pressure of 4000 psi using a hydraulic press as shown in Fig. 3.6.

Typically 0.90 and 0.80g fine powders are used to make each pellet- and toroid- shaped green body, respectively. A small drop of poly vinyl alcohol (PVA) is mixed as a binder for preparing each of the green body. The green samples are then sintered at different sintering temperatures, T_s , (1100, 1150, 1200, 1225, 1250°C) in the air for burning out the PVA and densification. The heating and cooling rates in these cases are the same. The sintered samples are then polished to remove roughness of the surface and any oxide layer formed during the sintering process.



Fig. 3.6 (a) Disk- and, (b) toroid- shaped samples.

3.4 Structural and Morphological Characterization

Phase identification and structural analysis of the prepared compositions are carried out using X-ray diffractometer. Surface morphology of all the samples is investigated using the Field Emission Scanning Electron Microscope (FESEM). The basic principles of these techniques are discussed in the following sections.

3.4.1 X-ray diffraction

Bragg reflection is a coherent elastic scattering in which the energy of the X-ray is not changed on reflection. If a beam of monochromatic radiation of wavelength λ is incident on a periodic crystal plane at an angle θ and is diffracted at the same angle as shown in Fig. 3.7, the Bragg diffraction condition for X-rays is given by

$$2d \sin\theta = n\lambda \quad (3.2)$$

where, d is the distance between crystal planes and n is the positive integer which represents the order of reflection. Eq. (3.2) is known as Bragg law. This Bragg law suggests that the diffraction is only possible when $\lambda \leq 2d$ [79]. The X-ray diffraction (XRD) provides substantial information on the crystal structure.

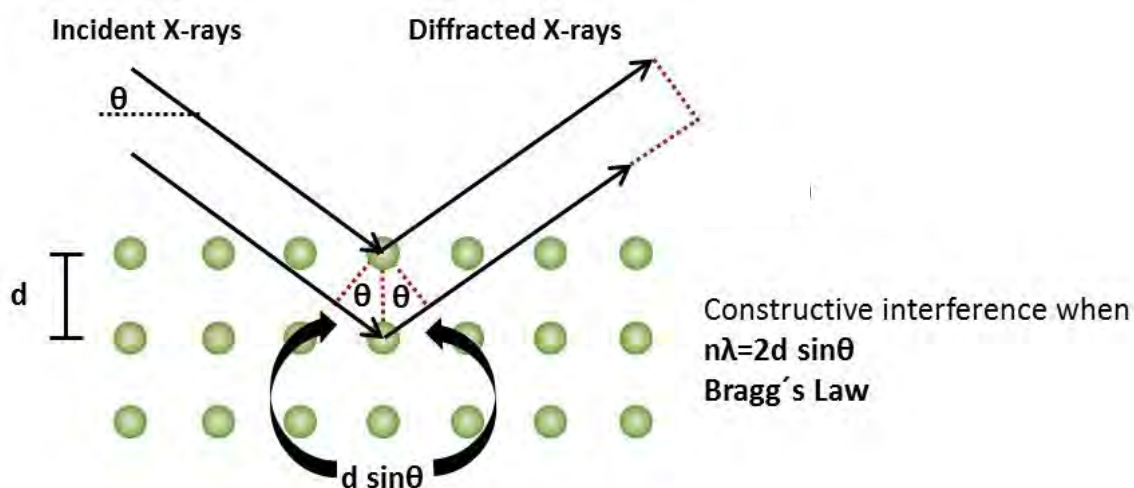


Fig 3.7 Bragg law of X-ray diffraction [80].

Here, X-ray diffraction is carried out with an X-ray diffractometer for the samples $\text{Mn}_{0.55}\text{Zn}_{0.45}\text{Ho}_x\text{Fe}_{2-x}\text{O}_4$. For this purpose monochromatic $\text{Cu-K}\alpha$ radiation is used. The lattice parameter for each peak of each sample was calculated by using the formula

$$a = d\sqrt{h^2 + k^2 + l^2} \quad (3.3)$$

where, h , k , and l are the indices of the crystal planes. To determine the exact lattice parameter for each sample, Nelson-Riley method was used. The Nelson-Riley function $F(\theta)$ is given as

$$F(\theta) = \frac{1}{2} \left[\left(\frac{\cos^2 \theta}{\sin \theta} \right) + \left(\frac{\cos^2 \theta}{\theta} \right) \right] \quad (3.4)$$

The values of lattice constant 'a' of all the peaks for a sample are plotted against $F(\theta)$. Then using a least square fit method exact lattice parameter 'a_o' is determined. The point where the least square fit straight line cut the Y-axis (i.e. at $F(\theta) = 0$) is the actual lattice parameter of the sample.

3.4.2 Density and porosity calculation

The bulk density, ρ_B , of the samples were determined by Archimedes principle in water medium using following expression [81]:

$$\rho_B = \frac{W\rho}{W - W'} \text{ g / cm}^3 \quad (3.5)$$

where, W is the weight of the sample in air, W' is the weight of the sample in the water and ρ is the density of water at room temperature.

However, in this thesis the experimental or bulk density of the selected compositions is calculated by using the following relation [82],

$$\rho_B = \frac{m}{\pi r^2 h} \quad (3.6)$$

where, r is the radius of the disc-shaped sample and h is the thickness of the pellet. The theoretical or X-ray density, ρ_{th} , of all the pellet shaped specimens is evaluated by using the following relation,

$$\rho_{th} = \frac{ZM}{N_A V} \quad (3.7)$$

where, Z denotes the number of formula unit per unit cell, M is the molecular weight, N_A is defined as the Avogadro's number (6.023×10^{23} /mole), and V is the volume of the unit cell.

The porosity of all the selected compositions is evaluated by using the following expression,

$$P(\%) = \left(\frac{\rho_{th} - \rho_B}{\rho_{th}} \right) \times 100 \quad (3.8)$$

3.4.3 Study of microstructure

The surface morphology of the sintered samples can be investigated by using a high resolution optical microscope, Scanning Electron Microscope (SEM), Field Emission Scanning Electron Microscope (FESEM) and Transmission Electron Microscope (TEM). SEM has been a powerful and popular tool for materials surface characterization. Electrons are used in electron microscope just like as the light or optical microscope which uses visible light for imaging. A SEM is a microstructure analysis tool which generates image of a sample by scanning the surface of the sample with a focused beam of electrons. The type of signals generated in SEM varies and can include characteristic X-rays, secondary electrons, and back scattered electrons. Fig. 3.8 shows the type of signals produced in SEM. The most general SEM mode is the detection of secondary electrons that are emitted by the atoms of the sample excited by the incident electron

beam. The resolution of SEM image is better than that of a light microscope since the wavelength of electrons is much smaller than the wavelength of light. The resolution of SEM image can be better than one nanometer [83].

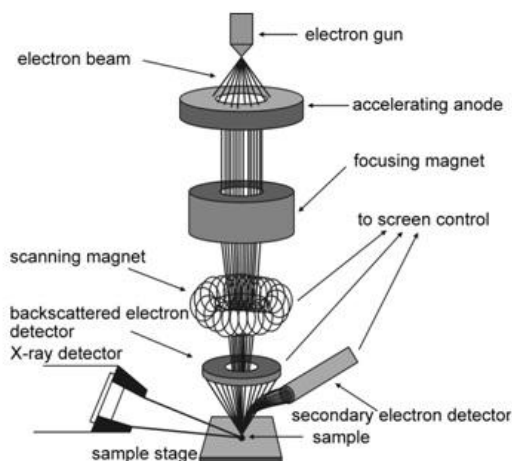


Fig. 3.8 Various types of signals which are generated by SEM [84].

FESEM is another microstructure analysis tool just like as SEM, provides useful information from the surface of a sample with higher resolution and much greater energy range than that of SEM. As like as SEM electron beam is used for scanning the sample surface. The main difference between a typical SEM and FESEM is the electron beam generation system. A field emission gun is used as a source of electrons in FESEM that produces extremely focused electron beam. For this reason, spatial resolution is improved greatly that enables the function to be performed at very low potentials (0.02-5 KV) [84]. In FESEM, Electrons are emitted from a field emission source. They are accelerated in a high electrical field gradient. Within the high vacuum column these so-called primary electrons are focused and deflected by electronic lenses to produce a narrow scan beam that bombards the object. As a result secondary electrons are emitted from every spot on the object. The velocity and angle of these secondary electrons are related to the surface structure of the sample. A detector catches the secondary electrons and produces an electronic signal which is amplified and transformed to a video scan-image that can be seen on a monitor or to a digital image that can be saved and processed further. In this thesis, the microstructural analysis of the surface of sintered samples is performed using the FESEM (JEOL, JSM-7600F) illustrated in Fig. 3.9.

From microstructure of the sample the d is evaluated by using the linear intercept technique through the relation, $d = 1.56 \lambda / \lambda$ [85]; where, λ is the average intercept length over a large number of grains as measured on the plane of the sample. For finding out the average intercept length several random vertical and horizontal lines are drawn on the micrograph of the selected sample. For ensuring the greater accuracy, at least fifty intercept lengths are measured in different places for each sample. Then the numbers of intercept length are counted and measured the length along the line traversed. Finally, d is evaluated.

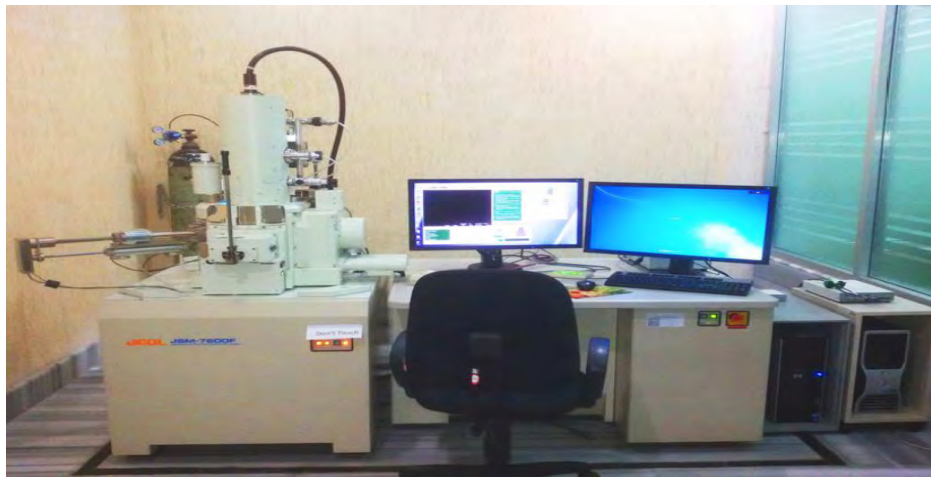


Fig. 3.9 FESEM setup.

3.4.4 Energy-dispersive X-ray spectroscopy

Energy-dispersive X-ray spectroscopy (EDX) is typically a quantitative analytical technique which is used for the chemical characterization or elemental analysis of a sample. EDX can be used to determine the chemical elements which are present in a given sample [86]. It can also be used to estimate the relative abundance of each element in the specimen.

3.5 Complex Initial Permeability Measurement

For high frequency application, the desirable property of a ferrite is high permeability with low loss. One of the most important goals of ferrite research is to fulfill this requirement. The techniques of permeability measurement and frequency characteristics of the present samples are described in sections 3.5.1 and 3.5.2.

3.5.1 Techniques for the initial permeability measurement

Measurements of permeability basically correspond to the measurements of the change in self-inductance of a coil in presence of the magnetic core [79]. The behavior of a self-inductance can be explained as follows:

Let us consider an ideal loss less air coil of inductance L_0 . On insertion of a magnetic core with μ , the inductance will be μL_0 . The complex impedance Z of this coil [45] can be expressed as follows:

$$Z = R + jX = j\omega L_0\mu = j\omega L_0(\mu' - j\mu'') \quad (3.9)$$

where, the resistive and reactive parts are given by,

$$R = \omega L_0\mu'' \quad (3.10)$$

$$X = \omega L_0\mu' \quad (3.11)$$

here, $\omega (= 2\pi f)$ defines the angular frequency. The permeability can be derived from the complex impedance (Z) of a coil given by Eq. 3.9. Generally, the core is taken as toroidal shape (Fig. 3.10) to avoid demagnetizing effects.



Fig. 3.10 Toroid shaped sample for the measurement of permeability.

3.5.2 Frequency dependent characteristics

The frequency dependent complex permeability of the selected compositions is investigated by using a precision impedance analyzer (Wayne Kerr Impedance Analyzer, 6500B). All the measurements are carried out at room temperature in the frequency range 20 Hz to 120 MHz. The μ_i' and μ_i'' are determined by using the following expressions [87],

$$\mu'_i = \frac{L_s}{L_0} \quad (3.12)$$

$$\mu''_i = \mu'_i \tan \delta \quad (3.13)$$

where, L_s defines the self-inductance of the sample core. L_0 is the inductance of the winding coil without the sample core which is derived geometrically by using the following relation,

$$L_0 = \frac{\mu_0 N^2 S}{\pi \bar{d}} \quad (3.14)$$

where, N is the number of turns of the coil ($N = 4$), S denotes the area of cross section of the toroid-shaped sample and \bar{d} is the mean diameter of the toroid- sample. The cross sectional area of the toroid-shaped sample can be calculated as follows,

$$S = d \times h \quad (3.15)$$

where,

$$d = \frac{d_2 - d_1}{2} \quad (3.16)$$

here d_1 is the inner diameter of the sample core, d_2 is the outer diameter of the sample core, and h is the thickness of the sample core.

The mean diameter of the toroid shaped sample can be calculated as,

$$\bar{d} = \frac{d_1 + d_2}{2} \quad (3.17)$$

The relative quality factor (RQF) is evaluated by using the following relation,

$$RQF = \frac{\mu'_i}{\tan \delta} \quad (3.18)$$

where, $\tan \delta$ (Quality factor; $Q = \frac{1}{\tan \delta}$) is the loss factor.

3.6 DC Magnetization Measurement Technique

Vibrating sample magnetometer (VSM) technique is used to measure the change of magnetization of materials as a function of an external field, which enables to identify their magnetic nature. It is a versatile and sensitive method of measuring magnetic properties developed by S. Foner and is based on the flux change in a coil when the sample is vibrated near it [87]. Paramagnetic, diamagnetic and ferromagnetic materials

will have a different reaction to the applied field. In ferromagnetic samples, a hysteresis loop is expected. The degree of bending of the M-H graph represents the amount of ferromagnetism in the examined sample. The principle of the VSM is, as its name reveals, based on the mechanical vibration of a magnetic sample in a homogeneous magnetic field, which will produce a change in the magnetic flux in the neighborhood of the sample. The sample is vibrating sinusoidally at small fixed amplitude with respect to stationary pick-up coils. According to Faradays law, an electromagnetic field will be induced, proportional to the rate of the flux change, as

$$V(t) \propto d\Phi_B / dt \quad (3.19)$$

VSM is designed to continuously measure the magnetic properties of materials as a function of temperature and field. In this type of magnetometer, the sample is vibrated up and down in a region surrounded by several pickup coils. The magnetic sample is thus acting as a time-changing magnetic flux, varying inside a particular region of fixed area. From Maxwell's law it is known that a time varying magnetic flux is accompanied by an electric field and the field induces a voltage in pickup coils. This alternating voltage signal is processed by a control unit system, in order to increase the signal to noise ratio. The result is a measure of the magnetization of the sample.

3.7 Dielectric Measurement Techniques

In this thesis, the measurements of dynamic (dielectric and electrical) transport properties are performed by using a precision Impedance Analyzer (Wayne Kerr Impedance Analyzer, 6500B). For electrical and dielectric measurement, the pellet shaped samples are first polished to remove roughness of the surface and contamination of any other oxides on the surface during the sintering process. Both sides of the samples are then painted with conducting silver paste for ensuring the good electrical contacts as illustrated in Fig. 3.11. The ϵ' of the selected samples is then calculated using the Eq. (2.17) [88],

$$\epsilon' = \frac{C}{C_0} \quad (3.20)$$

where, C is the capacitance of the sample measured by the Impedance Analyzer and C_0 is the capacitance of the same capacitor without the dielectric material.



Fig. 3.11 Silver paste painted two probe arrangements on the sintered sample.

The imaginary part of dielectric constant is calculated by using the following relation,

$$\varepsilon'' = \varepsilon' \tan \delta_E \quad (3.21)$$

where, ' $\tan \delta_E$ ' is known as the loss tangent.

3.7.1 Measurement of ac-conductivity

For understanding the mechanism of conduction the ac-conductivity of all the selected compositions are determined at room temperature for a wide range of frequency. The ac-conductivity can be calculated according to the following relation [89],

$$\sigma_{ac} = \frac{d}{(A \times R_{ac})} \quad (3.22)$$

where, R_{ac} is the ac resistance. The electrical conductivity of most of the materials is expressed as,

$$\sigma(\omega, T) = \sigma_{dc}(T) + \sigma_{ac}(\omega, T) \quad (3.23)$$

where, σ_{dc} defines the dc-conductivity which depends only upon the temperature and σ_{ac} is the ac-conductivity which depends both on the frequency and temperature. The frequency dependent ac-conductivity can be expressed by the empirical formula,

$$\sigma_{ac}(\omega, T) = A\omega^n \quad (3.24)$$

where, A and n both are constants which depend on temperature as well as composition. The constant n is dimensionless and A has units of σ_{ac} . The ac-conductivity of all the sintered samples are evaluated from the dielectric constant data by using the following expression [90],

$$\sigma_{ac} = \varepsilon' \varepsilon_0 \omega \tan \delta \quad (3.25)$$

where, $\omega (= 2\pi f)$ defines the angular frequency.

3.7.2 Impedance spectroscopy

The complex impedance spectroscopy is a powerful tool to investigate the electrical properties of the complex perovskite oxides [90-91]. The main advantages of the techniques are i) it involves relatively simple electrical measurements that can readily be automated ii) the measurements can be implemented by using arbitrary electrodes, iii) the results can be often correlated with the properties such as composition, microstructure, defects, dielectric properties, chemical reaction etc. of the sample, iv) the resistance of the grain boundaries and that of grains can be easily separated in most of the polycrystalline samples.

AC measurements are often made with a Wheatstone bridge type of apparatus (Impedance analyzer or LCR meter) in which the R and C of the sample are measured and balanced against variable resistors and capacitors. The impedance $|Z|$ and the phase difference (θ) between the voltage and current are measured as a function of frequency for the given sample and the technique is called impedance spectroscopy. Analysis of the data is carried out by plotting the imaginary part of the impedance $Z'' = |Z| \cos\theta$ against the real part $Z' = |Z| \sin\theta$ on a complex plane called the impedance plot. An impedance plot with linear scale is used to analyze the equivalent circuit as follows. Impedance plot of a pure resistor is a point on real axis and that of pure capacitor is a straight line coinciding with the imaginary axis. The impedance of a parallel RC combination is expressed by the following relation [69]:

$$Z^* = Z' - jZ'' = \frac{R}{(1 + j\omega RC)} \quad (3.26)$$

After simplification, one gets

$$\left(Z' - \frac{R}{2}\right)^2 + (Z'')^2 = \left(\frac{R}{2}\right)^2 \quad (3.27)$$

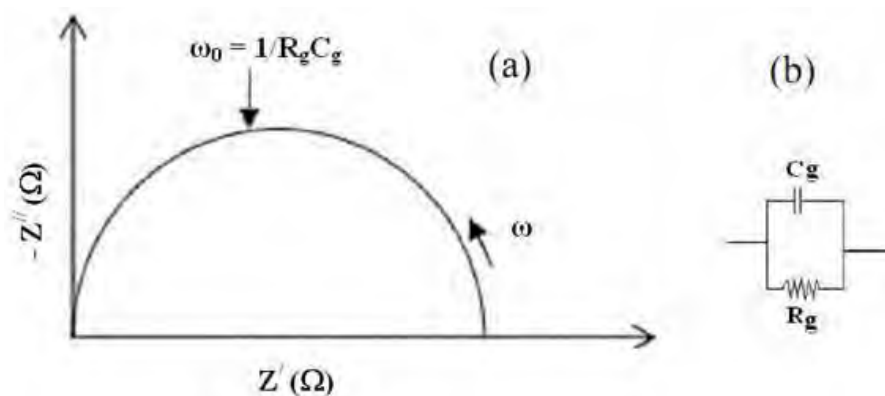


Fig. 3.12 (a) The impedance plot for a circuit of a resistor and a capacitor in parallel and (b) the corresponding equivalent circuit [92].

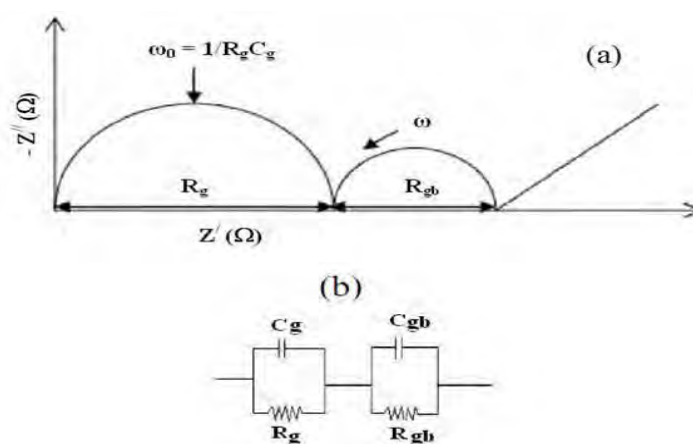


Fig. 3.13 (a) The impedance plot for an ideal polycrystalline sample and (b) the corresponding equivalent circuit [92].

Which represents the equation of a circle with radius $R/2$ and center at $(R/2, 0)$. Thus, a plot of Z' vs. Z'' (as parametric function of ω) will result in a semicircle (Fig. 3.12 and 3.13) of radius $R/2$. This plot is often called a Nyquist plot. The time constant of the simple circuit is defined as

$$\tau = RC = \frac{1}{\omega_0} \quad (3.28)$$

3.7.3 Modulus spectra

The study of complex modulus spectroscopy provides crucial information about the distribution parameters of different micro regions in the polycrystalline sample such as grain, grain boundary and electrode interface. This technique is very effective in separating the contributions of different factors such as grain boundary effect, bulk effect and interfaces. It is also useful for separating the components having similar resistance but quite different capacitance. The real and imaginary part of the electric modulus are obtained from the impedance data according to the following relations [68],

$$M' = \frac{\varepsilon'}{(\varepsilon'^2 + \varepsilon''^2)} = \omega C_0 Z'' \quad (3.29)$$

$$M'' = \frac{\varepsilon''}{(\varepsilon'^2 + \varepsilon''^2)} = \omega C_0 Z' \quad (3.30)$$

4. RESULTS AND DISCUSSION

In the present research Ho^{3+} substituted $\text{Mn}_{0.55}\text{Zn}_{0.45}\text{Ho}_x\text{Fe}_{2-x}\text{O}_4$ (with $x=0.00, 0.03, 0.06, 0.09$ and 0.12) are synthesized by the standard solid state reaction technique. Structural characterization, density, porosity, compositional analysis, microstructural characterization, and various electromagnetic properties are thoroughly investigated.

4.1 Samples Sintering Temperature and Density

Samples prepared from $\text{Mn}_{0.55}\text{Zn}_{0.45}\text{Ho}_x\text{Fe}_{2-x}\text{O}_4$ powders sintered at various T_s (1100, 1150, 1200, 1225, 1250°C) in air for 5 hours. Density plays a key role in controlling different properties of ferrites. Variation of ρ_B with Ho^{3+} contents for the sample sintered at various T_s is shown in Fig. 4.1. From this figure it is shown that density decreases with increasing Ho^{3+} content. On the other hand, density increases with increasing T_s up to 1225°C and then decreases with further increasing T_s .

Fig. 4.1 Variation of ρ_B with Ho^{3+} contents of various $\text{Mn}_{0.55}\text{Zn}_{0.45}\text{Ho}_x\text{Fe}_{2-x}\text{O}_4$ for various T_s .

From this result it is concluded that the optimum T_s for these ferrites is 1225°C. Therefore, samples sintered at 1225°C are considered for further investigation.

4.2 X-ray Diffraction Analysis

The formation of spinel structure of various polycrystalline $\text{Mn}_{0.55}\text{Zn}_{0.45}\text{Ho}_x\text{Fe}_{2-x}\text{O}_4$ was confirmed by XRD. XRD pattern of $\text{Mn}_{0.55}\text{Zn}_{0.45}\text{Ho}_x\text{Fe}_{2-x}\text{O}_4$ is shown in Fig.4.2. All diffraction peaks for the samples correspond to fairly spinel lattice with a cubic structure [93]. Some traces of raw material (HoFeO_3) were found, due to larger ionic radius of Ho^{3+} (1.04 Å) relative to Fe^{3+} (0.67 Å) it cannot totally enter into the ferrite lattice [62]. Some Ho^{3+} may reside at the grain boundaries and form HoFeO_3 indicated by (*) (ICDD card: 01-074-1479). On the other hand, a gradual increase in the intensity of the impurity peak is noticed with increasing Ho^{3+} content.

Fig.4.2 XRD patterns of various $\text{Mn}_{0.55}\text{Zn}_{0.45}\text{Ho}_x\text{Fe}_{2-x}\text{O}_4$.

The appearance of secondary phase might be due to the isolation of Ho^{3+} at the grain boundaries, signifying the solubility of Ho^{3+} into the spinel structure [57]. Precipitation of the secondary phase at the grain boundary reduces the grain growth and increases the resistivity. This means that the formation of secondary phases in the ferrite during sintering process is governed by the type and the amount of Ho^{3+} used. Therefore, the small amounts of Ho^{3+} in Mn–Zn ferrite affect not only the phase composition but also the grain size of the spinel matrix. The impurity peaks are mainly from the unreacted ingredients of these compositions.

4.3 Lattice Parameters

The values of a_0 have been calculated with the help of the Nelson-Riley function [Eq. 3.4]. The value of lattice parameters are estimated from the extrapolation of these lines to $F(\theta) = 0$ or $\theta = 90^\circ$. The samples under investigation have the chemical composition $\text{Mn}_{0.55}\text{Zn}_{0.45}\text{Ho}_x\text{Fe}_{2-x}\text{O}_4$. Therefore, the ionic radius of the variant ions for composition can be written as $r_{(\text{variant})} = x r_{\text{Ho}^{3+}} + (2-x)r_{\text{Fe}^{3+}}$ [94], where $r_{\text{Ho}^{3+}}$ is the ionic radius of Ho^{3+} and $r_{\text{Fe}^{3+}}$ is the ionic radius of Fe^{3+} .

The variation of a_0 with Ho^{3+} content is shown in the Table 4.1. An increase of a_0 with increasing Ho^{3+} content is expected because of the large ionic radius of Ho^{3+} compared to that of Fe^{3+} . It is expected that Ho^{3+} enter into the octahedral sites in place of Fe^{3+} which could results an internal stress to make the lattice distorted and an expansion of unit cell [95, 96]. The values of a_0 (8.4700-8.4750 Å) are also in good agreement with the earlier reported value [97].

Fig. 4.3 Variation of a_0 with Ho^{3+} content of various $\text{Mn}_{0.55}\text{Zn}_{0.45}\text{Ho}_x\text{Fe}_{2-x}\text{O}_4$.

It is possible that some of the Ho^{3+} enter into the spinel lattice during sintering and activate the lattice diffusion. This assumption of the formation of solid solution is confirmed by a_0 . The increase of the lattice diffusion usually increases the diffusion path, leading to an increase of the rate of cation inter diffusion in the solid solution which is in agreement with the lattice diffusion mechanism proposed by Gupta and Coble [98].

4.4 Porosity

Fig. 4.4 shows the variation of density and porosity with Ho^{3+} content for the samples sintered at 1225°C .

Fig. 4.4 Variation of ρ_{th} , ρ_B , and P with Ho^{3+} content of various $\text{Mn}_{0.55}\text{Zn}_{0.45}\text{Ho}_x\text{Fe}_{2-x}\text{O}_4$ sintered at 1225°C .

Table 4.1 Data of ρ_{th} , ρ_B and P of various $\text{Mn}_{0.55}\text{Zn}_{0.45}\text{Ho}_x\text{Fe}_{2-x}\text{O}_4$ samples.

content (x)	a_0 (Å)	ρ_{th} (g/cm ³)	ρ_B (g/cm ³)	P (%)
0.00	8.4700	5.75	4.75	17
0.03	8.4742	5.80	4.51	22
0.06	8.4744	5.85	4.48	23
0.09	8.4748	5.87	4.47	24
0.12	8.4750	5.91	4.45	25

It is observed from Fig. 4.4 that the ρ_{th} increased from 5.75 to 5.90 g/cm³ with increasing Ho^{3+} substitution and this behavior of ρ_{th} is related to the M_A and a_0 . The increase in ρ_{th} may be due to the greater M_A of Ho^{3+} (164.93 amu) compared to that of Fe^{3+} (55.85 amu). From Fig. 4.4, ρ_B was found to be lower than that of the ρ_{th} which might be due to the existence of pores, which were created during the sintering process [57]. The ρ_B decreased with Ho^{3+} content because of large sized Ho^{3+} do not enter in the spinel lattice. It is also seen from Fig. 4.4 that the variation of P with Ho^{3+}

content followed the opposite trend of ρ_B . The value of ρ_{th} , ρ_B and P of the various $Mn_{0.55}Zn_{0.45}Ho_xFe_{2-x}O_4$ are tabulated in Table 4.1.

4.5 Microstructural Analysis

The microstructure of ferrites strongly influences their electrical and magnetic properties, so it is necessary to determine the average grain size, λ , and the type of grain growth of the samples.

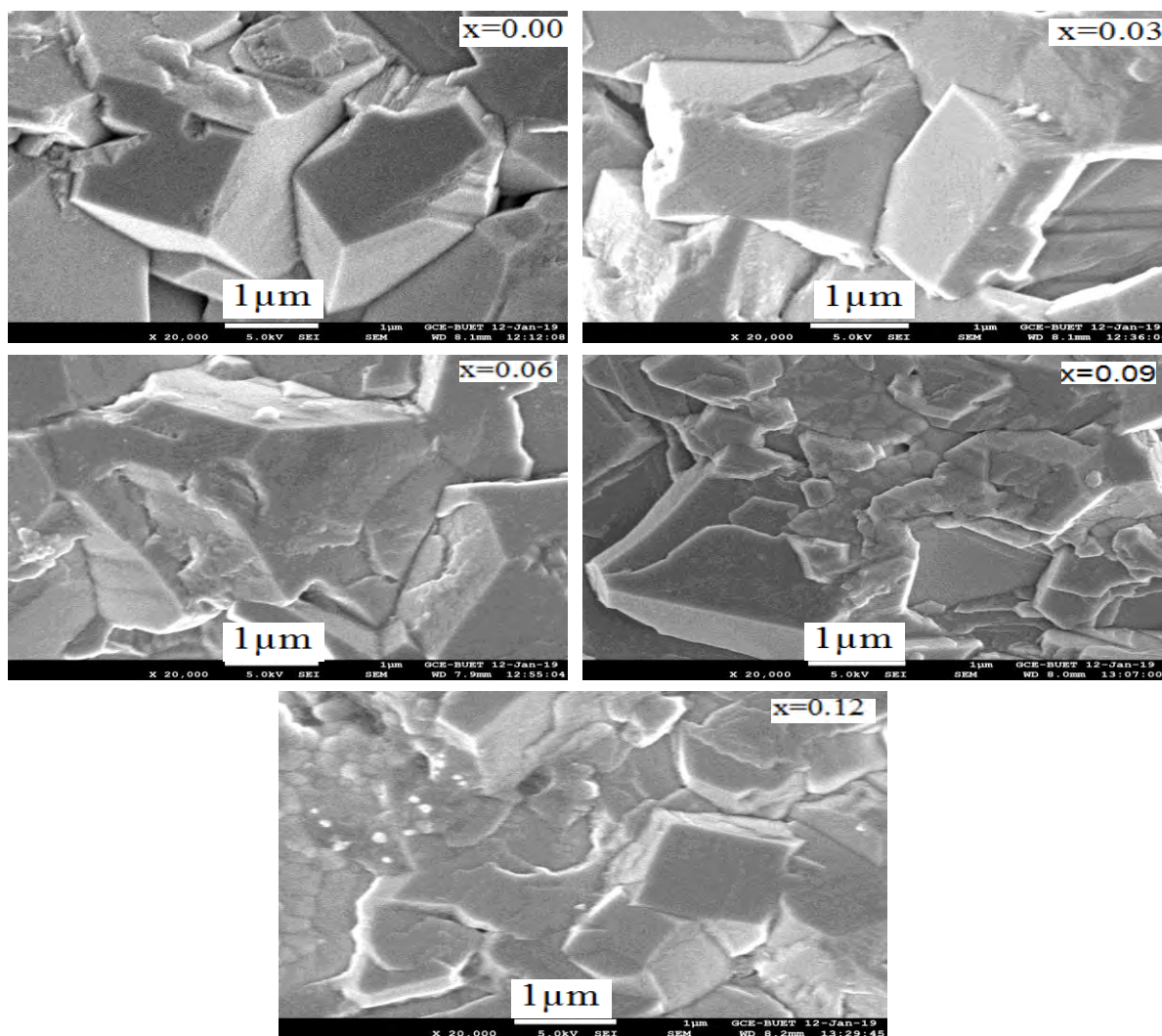


Fig. 4.5 The microstructure of various $Mn_{0.55}Zn_{0.45}Ho_xFe_{2-x}O_4$ samples sintered at 1225°C .

All the compositions contain randomly aligned non-uniform grains in size and shape due to very high sintering temperature. The distribution of grains is not homogeneous and some agglomeration is appeared in higher doped samples. Non-equivalent size of

dopant ions may be the reason behind this agglomeration of grains. The FESEM micrographs of various $\text{Mn}_{0.55}\text{Zn}_{0.45}\text{Ho}_x\text{Fe}_{2-x}\text{O}_4$ samples sintered at 1225°C with different magnifications are shown in Fig. 4.5. All the samples show a dense microstructure. It is evident from these images that the Ho^{3+} substitution induces changes in the microstructure of $\text{Mn}_{0.55}\text{Zn}_{0.45}\text{Ho}_x\text{Fe}_{2-x}\text{O}_4$. It is observed that the d is increased with Ho^{3+} content up to $x=0.03$ and then decreased for further increasing Ho^{3+} content. The P reflects the presence of more or less grain boundary area. Even P may be strongly related to d because the lower stress is created high P of the ferrite which may lead to an increment of d with the ferrite content. The uniformity and the grain size and the average grain diameter can control properties such as the magnetic permeability. The value of d of different compositions is obtained by using the linear intercept method. d values are decreasing from $1.48 \mu\text{m}$ to $0.84 \mu\text{m}$, with substitution of Ho^{3+} . Because in this case significant amount of Ho^{3+} reside at the grain boundaries which hamper the grain growth and may be increased in strain on the grains [99], consequently, leads to decrease of d . The behavior of grain growth reflects the competition between the driving force for grain boundary movement and the retarding force exerted by pores [99]. During the sintering process, the thermal energy generates a force that drives the grain boundaries to grow over pores, thereby decreasing the pore volume and densifying the material.

4.6 Energy Dispersive Spectroscopy Analysis

Energy dispersive spectroscopy (EDS) analyses of various $\text{Mn}_{0.55}\text{Zn}_{0.45}\text{Ho}_x\text{Fe}_{2-x}\text{O}_4$ are collected from FESEM to calculate and determine the composition. The identified peaks are generated from Mn, Zn, Ho, Fe and O that form the $\text{Mn}_{0.55}\text{Zn}_{0.45}\text{Ho}_x\text{Fe}_{2-x}\text{O}_4$. The percentages of elements present in compositions are listed in the attached table of the EDS spectra. The EDS spectra also taken at different points of the sample provide quantitative elemental analysis as presented in Fig 4.6. It is found from EDS spectra that there exist a well consistency between the mass percentage of the elements in the component phase and nominal composition of the corresponding phase.

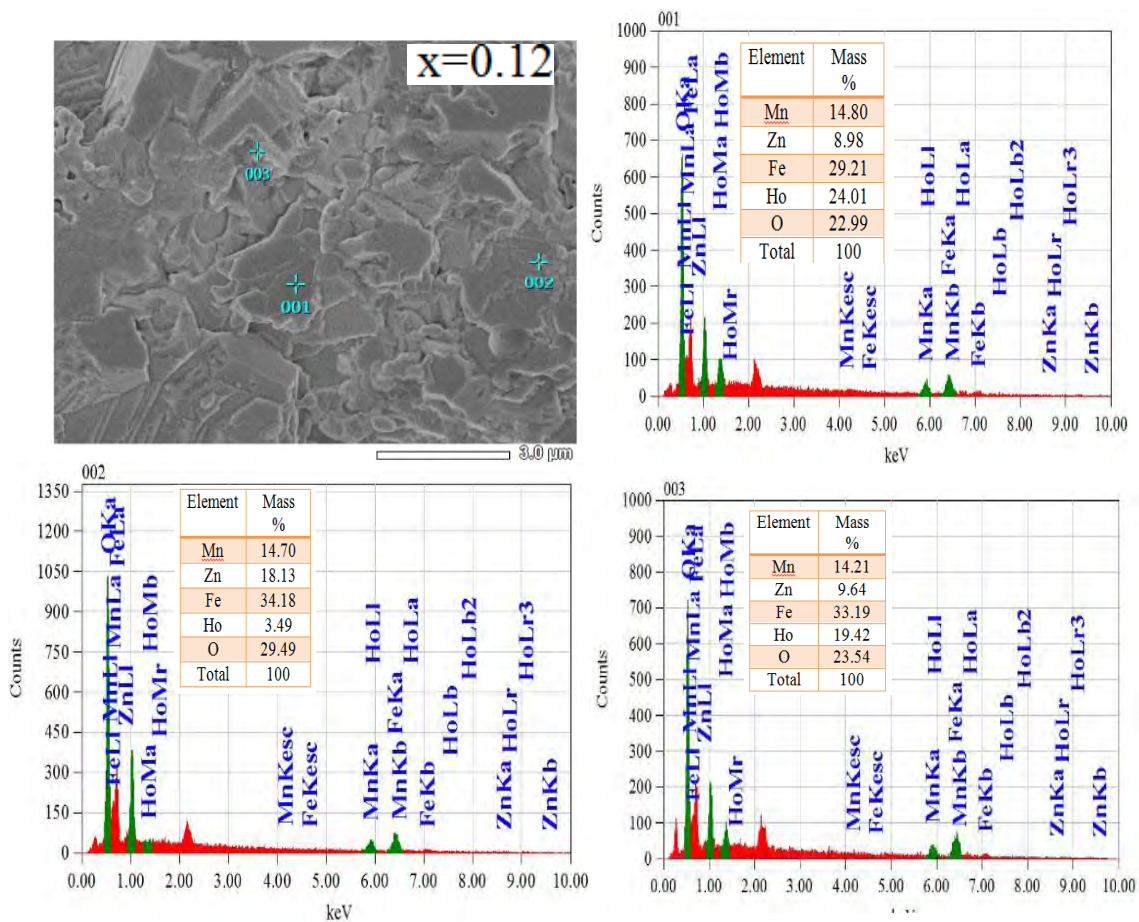


Fig. 4.6 FESEM images along with EDS spectrum of $x=0.00$, $x=0.03$, $x=0.06$, $x=0.09$, and $x=0.12$ samples of $\text{Mn}_{0.55}\text{Zn}_{0.45}\text{Ho}_x\text{Fe}_{2-x}\text{O}_4$ sintered at 1225°C .

4.7 Magnetic Properties

4.7.1 Complex initial permeability

The complex initial permeability is an important magnetic parameter to have information about the dynamic properties and adaptability of a magnetic material in high frequency. The complex initial permeability is usually given by, $\mu_i^* = \mu_i' - i\mu_i''$, where μ_i' and μ_i'' are defined as the real and imaginary parts of complex initial permeability. μ_i' expresses the component of magnetic induction B in phase with the alternating magnetic field H and typically used to denote the magnetic energy that store in the system. Fig. 4.7 shows the variation of μ_i' with frequency of various $\text{Mn}_{0.55}\text{Zn}_{0.45}\text{Ho}_x\text{Fe}_{2-x}\text{O}_4$ samples within the range of frequency of 10 kHz – 120 MHz at room temperature respectively. As shown in Fig. 4.7, the value of μ_i' for all the compositions remains almost constant up to certain frequency and then decreases with increasing frequency. The value of μ_i' decreases with frequency which is due to the

fact that at higher frequencies, pinning points are found to be originated at the surface of the samples from the impurities of grains and intragranular pores. The pinning points exist both at lower as well as higher frequency. At higher frequency, the motion of domain wall is obstructed more by the pinning points because of rapidly changing magnetic field. This phenomenon in turn obstructs the motion of spin and domain walls and the contribution of their motion towards the increment of permeability decreases and thereby the permeability decreases [100]. It is also known that Zn, Ho and Mn occupy A-sites, although Fe and Mn exist at both A- and B- sites [101, 93]. When Ho^{3+} is introduced at the cost of Fe^{3+} , Fe^{3+} concentration at B sites increases. As Fe^{3+} is less magnetic material ($3.63\mu_B$) then the Ho^{3+} ($10.6\mu_B$), so when Ho^{3+} content increases in the A site of the present ferrites, Fe content decreases in A- site. As a result, the magnetic moments of B- sub-lattice decreases. However, as Ho^{3+} content increases, the magnetic moment of A sub-lattice increases. As the net magnetization equals M_B minus M_A , it decreases with increasing Ho concentration.

On the other hand, it is observed that the value of μ'_i of all samples are found independent of frequency below the resonance frequency. It is also found that as μ'_i increases resonance frequency (f_r) decreases with the function of T_s . An inversely proportional relation of μ'_i and f_r confirms the Snoek's law [102], that relates the permeability with resonance frequency as,

$$\mu'_i f_r = \text{constant} \quad (5.1)$$

This relation implies that the larger the value of μ'_i the smaller the value of f_r .

Natural resonance peak has been observed for some samples. No resonance peak is observed for rest of the samples. One possible reason can be their ferromagnetic f_r that lies beyond the measured frequency range. However, the reason behind that the arrangement of the magnetic moment can follow the variation of external magnetic field for a longer time during the process of magnetization and thus the value of μ'_i may shows stable value for a certain period of time [103]. Stable value of μ'_i with frequency is important and it has potential applications in several electrical devices such as broad band transformer and wide band read-write head for video recording etc [104, 105].

Fig. 4.7 The μ_i' spectra for various $\text{Mn}_{0.55}\text{Zn}_{0.45}\text{Ho}_x\text{Fe}_{2-x}\text{O}_4$ sintered at different T_s .

The permeability of ferrite is related to two different magnetizing factors: spin rotation and domain wall motion [106, 107], which can be described as: $\mu_i' = 1 + \chi_w + \chi_{spin}$ where χ_w is the domain wall susceptibility; χ_{spin} is intrinsic rotational susceptibility. χ_w and χ_{spin} may be written as: $\chi_w = \frac{3\pi M_s^2 D}{4\gamma}$ and $\chi_{spin} = \frac{2\pi M_s^2}{K}$ with M_s saturation magnetization, K the total anisotropy, D the average grain diameter, and γ the domain wall energy [108]. Thus, the domain wall motion is affected by the grain size and

enhances with the increase of d . The initial permeability is therefore a function of d . Larger grains tend to consist of a greater number of domain walls. The magnetization caused by domain wall movement requires less energy than that required by domain rotation. As the number of walls increases with the d , the contribution of wall movement to magnetization is increased. Therefore in the present case, variation of the initial permeability is strongly influenced by its d and P .

It is difficult to explain compositional dependence of μ'_i for the case of polycrystalline materials because μ'_i is sensitive to many factors. The value of μ'_i depends on stoichiometry, composition, average grain size, impurity, coercivity, density and porosity etc. The variation of μ'_i with Ho^{3+} content for $\text{Mn}_{0.55}\text{Zn}_{0.45}\text{Ho}_x\text{Fe}_{2-x}\text{O}_4$ samples sintered at different T_s , at three fixed frequencies are shown in Fig. 4.8. The variation of μ'_i at three fixed frequencies (1 kHz, 10 kHz, and 1 MHz) shows almost similar behavior.

Fig. 4.8 The variation of μ'_i (a) at 1 kHz, (b) at 10 kHz, and (c) at 1 MHz with Ho^{3+} content for $\text{Mn}_{0.55}\text{Zn}_{0.45}\text{Ho}_x\text{Fe}_{2-x}\text{O}_4$ sintered at different T_s .

4.7.2 Loss factor

Energy loss is an extremely important subject in soft ferrimagnetic materials, since the amount of energy wasted on process other than magnetization can prevent the AC applications of a given material. The ratio of μ_i'' and μ_i' representing the losses in the material is a measure of the inefficiency of the magnetic system. Obviously this parameter should be as low as possible. The magnetic losses, which cause the phase shift, can be split up into three components: hysteresis losses, eddy current losses and residual losses. This gives the formula $\tan\delta_m = \tan\delta_h + \tan\delta_e + \tan\delta_r$. Hysteresis losses vanish at very low field strengths. As the value of μ_i' which is measured in presence of low applied magnetic field. Thus at low field the remaining magnetic losses are due to eddy current losses and residual losses. Residual losses are independent of frequency. Eddy current losses increase with frequency and are negligible at very low frequency. Eddy current loss can be expressed as, $P_e \approx f^2/\rho$, where P_e is the energy loss per unit volume and ρ is the resistivity [67, 109]. To keep the eddy current losses constant as frequency is increased, the resistivity of the material chosen must increase as the square of frequency. Eddy currents are not problem in the Mn-Zn ferrites until higher frequencies are encountered because they have very high resistivity about $10^5 \Omega\text{cm}$ to $10^8 \Omega\text{cm}$ [110]. The ferrite microstructure is assumed to consist of grains of low resistivity separated by grain boundaries of high resistivity. Thicker grain boundaries are preferred to increase the resistance.

The variation of loss $\tan\delta_M$ with frequency for all samples has been studied. Fig.4.9 shows the variations of loss factors with frequency for $\text{Mn}_{0.55}\text{Zn}_{0.45}\text{Ho}_x\text{Fe}_{2-x}\text{O}_4$ samples sintered at 1100, 1150, 1200, 1225, and 1250°C. At lower frequencies dispersion in magnetic loss is observed and remains constant up to certain a frequency, this frequency limit depends upon the sintering temperature. The lag of domain wall motion with respect to the applied magnetic field is responsible for magnetic loss and this is accredited to lattice imperfections [111]. The decrease of $\tan\delta_M$ with frequency might be attributed to spin inversion losses as suggested by Gama and Rezende [112] or due to the reduction of activity of space charges because space charges cannot follow the rapid variation of the field at high frequency. The values of $\tan\delta_M$ for all the compositions are found decreasing very significantly and it may be due to the reduction of imperfection with Ho^{3+} substitution.

Fig. 4.9 Variation of $\tan\delta_M$ with frequency for $\text{Mn}_{0.55}\text{Zn}_{0.45}\text{Ho}_x\text{Fe}_{2-x}\text{O}_4$ sintered at different T_s .

4.7.3 Relative quality factor

The variation of RQF, for $\text{Mn}_{0.55}\text{Zn}_{0.45}\text{Ho}_x\text{Fe}_{2-x}\text{O}_4$ is shown in Fig. 4.10. The RQF is used as a performance indicator for practical applications. It is shown that the RQF increases with increase of frequency and peaks at a certain value and then decreases.

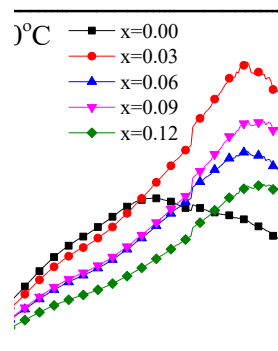


Fig. 4.10 Variation of RQF with frequency for $\text{Mn}_{0.55}\text{Zn}_{0.45}\text{Ho}_x\text{Fe}_{2-x}\text{O}_4$ sintered at different T_s .

But the peak is narrow and broadened with increasing Ho^{3+} content in the ferrite which increasing the frequency utility range, discloses that the loss of the samples at high frequency is quite low. It is observed that the sample sintered at 1225°C has highest Q value (~ 6652) for $x=0.03$ of $\text{Mn}_{0.55}\text{Zn}_{0.45}\text{Ho}_x\text{Fe}_{2-x}\text{O}_4$.

4.7.4 Hysteresis loop analysis

Fig. 4.11 shows the typical magnetic hysteresis curves for $\text{Mn}_{0.55}\text{Zn}_{0.45}\text{Ho}_x\text{Fe}_{2-x}\text{O}_4$ samples. From the hysteresis loop at room temperature, the saturation magnetization (M_s), coercivity (H_c) and Retentivity (M_r) were calculated and listed in Table 4.2. The values of M_s were found to be decreased with the increase of Ho^{3+} doped content for all the samples which might be due to the value of effective magnetic moment and radii of Ho^{3+} ions. Small quantity of Fe^{3+} ions at spinel lattice was substituted by Ho^{3+} ions on B sites. The exchange interactions may decrease with the increase of the Ho^{3+} content. The content of Fe^{3+} ions at ferrite lattice sites was decreased resulting to the decrease in magnetization due to the decrease of the strong Fe^{3+} - Fe^{3+} interactions. The values of H_c were found to be gradually increased with the increase in Ho^{3+} except $x = 0.06$. With the increase in Ho^{3+} doped content, the residing amount of Ho^{3+} ions at grain boundaries were increased resulted the movement of domain walls more difficult, and hence the coercivity was increased with the Ho^{3+} doped content [96].

Table 4.2 Data of M_s , H_c , M_r , n_B , and K_u of various $\text{Mn}_{0.55}\text{Zn}_{0.45}\text{Ho}_x\text{Fe}_{2-x}\text{O}_4$.

Content, x	Magnetization, M_s (emu/g)	Coercivity, H_c (Oe)	Retentivity, M_r (emu/g)	n_B (μ_B)	Anisotropy, K_u
0.00	71	21	4	2.9	752
0.03	51	47	5	2.2	1211
0.06	50	33	4	2.2	821
0.09	48	60	6	2.1	1442
0.12	44	70	7	1.9	1543

The number of Bohr magneton (n_B) is determined by the following relation: $n_B = \frac{M_A \times M_S}{N_A \times \mu_B}$ where, μ_B is the Bohr magneton ($= 9.27 \times 10^{-21}$ emu). The calculated values of n_B are tabulated in Table 4.2. The anisotropy constant, K_u was calculated using the relation $K_u = \frac{H_c M_S}{2}$ [13] and assuming the magnetic particles to be isolated (exchange interacting spin) single domains [113]. The values of K_u were found to be very less than that reported in RE doped CoFe_2O_4 [96] and showed that grains were no single domains and anisotropy contribution was not uniaxial, but it might be cubic magneto-crystalline anisotropy and hence strong grain to grain interactions were existed in these materials.

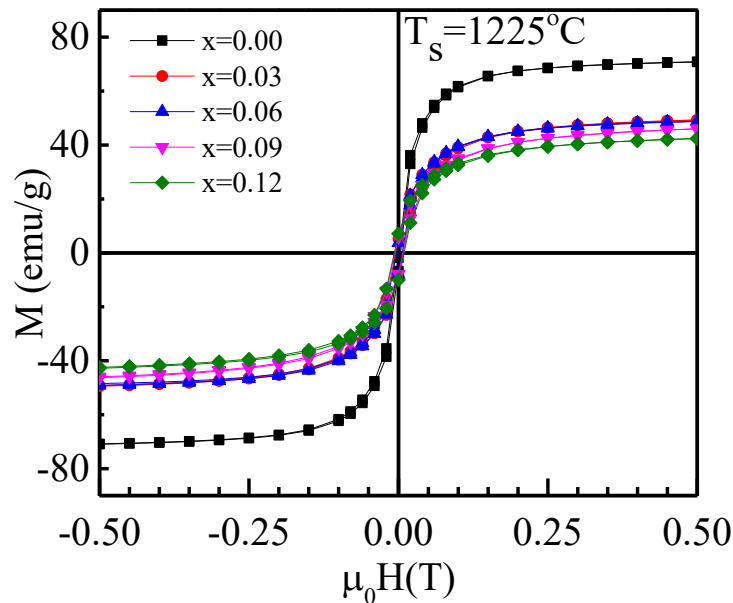


Fig. 4.11 M - H curves for various $\text{Mn}_{0.55}\text{Zn}_{0.45}\text{Ho}_x\text{Fe}_{2-x}\text{O}_4$.

4.8 Dielectric Properties

4.8.1 Dielectric constant

Frequency dependent real part of dielectric constant (ϵ') of $\text{Mn}_{0.55}\text{Zn}_{0.45}\text{Ho}_x\text{Fe}_{2-x}\text{O}_4$ is shown in Fig. 4.12. It is evident that at lower frequency all the compositions exhibit higher values of dielectric constant. It is observed that ϵ' decreases with the increase in frequency up to a certain value. Afterwards, it remains almost constant for all compositions. This low-frequency dielectric dispersion results because at low-frequency all types of polarizations (electronic, interfacial, dipolar and ionic) are

present in the samples. However, on increasing frequency some of the polarizations gradually disappear (except electronic and ionic) resulting in a rapid drop of ϵ' . The ϵ' remains almost constant at higher frequencies as the electric dipoles do not get enough time to line up and therefore cannot follow the rapid variation of the applied alternating electric field. In the low-frequency region, the large value of ϵ' results from the interfacial polarization suggested by Maxwell–Wagner [114-116]. According to this model, the dielectric materials are assumed to be composed of conducting grains separated by poorly conducting grain boundaries. The mechanism of polarization in ferrite is reported to be the hopping of electrons between ions of the same element in different oxidation states at B-site [117-119]. When an external electric field is applied on a dielectric medium the charge carriers begin to migrate through the conducting grain and are piled up at the resistive grain boundaries.

Fig. 4.12 Variation of ϵ' with frequency for $\text{Mn}_{0.55}\text{Zn}_{0.45}\text{Ho}_x\text{Fe}_{2-x}\text{O}_4$ sintered at different T_s .

As a result, large polarization takes place within the dielectric medium resulting high dielectric constant. In this case the poorly conducting grain boundaries contribute to the higher value of ϵ' at lower frequency. However, the polarization is affected by some other factors such as structural homogeneity, stoichiometry, grain size, density and porosity of the samples. In the present study, it is observed that the values of ϵ' decrease with the increase of Ho^{3+} content except $x=0.03$ sample as shown in Fig.4.12.

4.8.2 Dielectric loss factor

The inherent dissipation of electromagnetic energy as a form of heat from a dielectric material is defined as the dielectric loss. There are two forms of loss in a dielectric medium. In conduction loss, the energy dissipation is caused by flowing of charge through a material. On the other hand, in dielectric loss the dissipation of energy is caused by the movement of charges in an alternating electromagnetic field as polarization switches direction.

Fig. 4.13 Variation of $\tan\delta_E$ with frequency for $\text{Mn}_{0.55}\text{Zn}_{0.45}\text{Ho}_x\text{Fe}_{2-x}\text{O}_4$ sintered at different T_s .

Dielectric loss is high at the resonance or relaxation frequencies of the polarization mechanisms as the polarization lags behind the applied field, causing an interaction between the field and the dielectric's polarization that results in heating [120]. Materials having higher dielectric constants generally show higher dielectric loss.

The frequency dependent dielectric loss factor ($\tan\delta_E$) of $\text{Mn}_{0.55}\text{Zn}_{0.45}\text{Ho}_x\text{Fe}_{2-x}\text{O}_4$ sintered at various T_s 1200, 1225 and 1250°C is illustrated in Fig. 4.13. It is observed that at low frequency region the $\tan\delta_E$ is maximum and with the increase in frequency $\tan\delta_E$ is gradually decreased. The domain wall motion is suppressed at higher frequency and magnetization is changed by rotation resulting lower loss at higher frequency. However, there also appears some broad relaxation peaks at high frequency region indicating the existence of Debye-like relaxation [121]. Under the influence of externally applied field, the electric dipoles tend to align with the electric field. But the alignment is not happened instantaneously. The dipoles take some time to align with the field. This phenomenon is known as dipole relaxation. When the relaxation or resonance frequency is equal to the applied frequency, a maximum in loss tangent may be occurred.

4.8.3 The ac-Conductivity

For comprehending the conduction mechanism in different materials ac-conductivity (ζ_{ac}) is a crucial parameter. The σ_{ac} of the studied compositions sintered at various T_s 1200, 1225 and 1250°C is illustrated in Fig. 4.14. The value of σ_{ac} of all the sintered samples is found almost constant at low frequency region. Whereas the value of ζ_{ac} is increased very fast after a certain frequency. In low frequency region, the conductivity is almost independent of frequency because in this region the resistive grain boundaries are very active according to the Maxwell Wagner double layer model [122, 123]. On the other hand in high frequency region (hopping region), the conductivity increases faster because of the very active conductive grains thereby enhances hopping of charge carriers that contributes to the rise in conductivity. Therefore, the transport phenomenon occurs through penetrating process in low frequency zone, whereas in high frequency zone the transport phenomena is kept up by hopping carriers that are generated from the substituted elements [124].

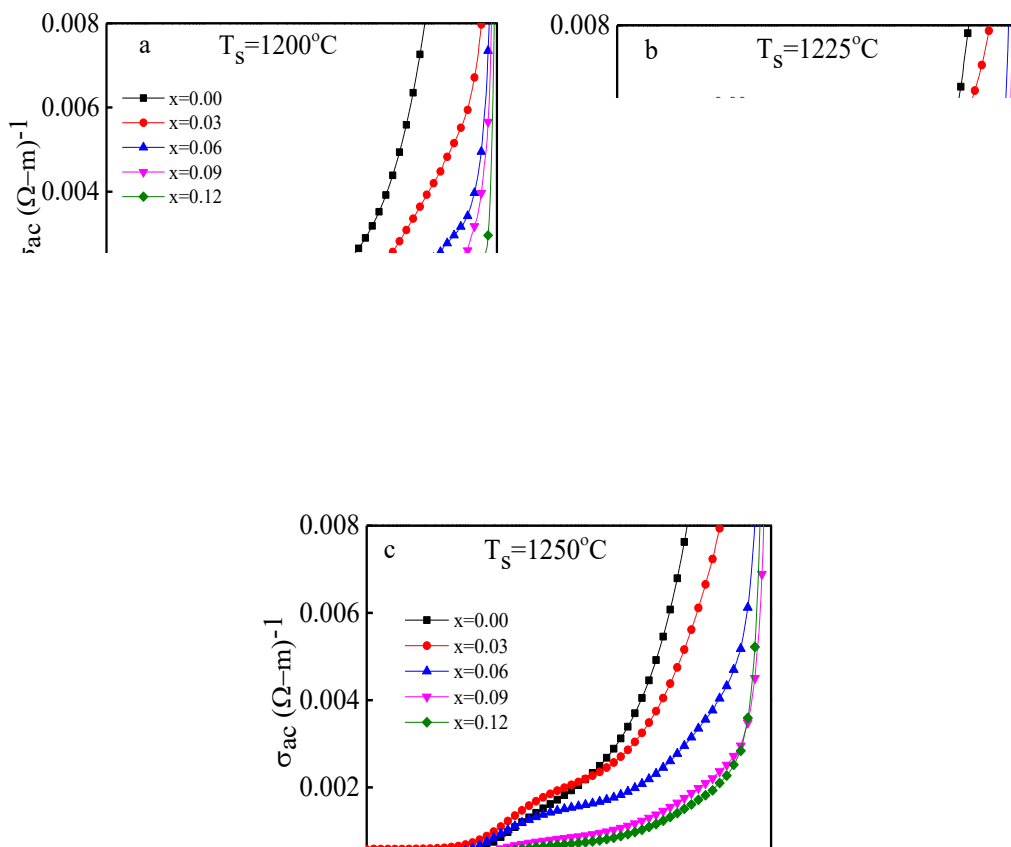


Fig. 4.14 Variation of σ_{ac} with frequency for $\text{Mn}_{0.55}\text{Zn}_{0.45}\text{Ho}_x\text{Fe}_{2-x}\text{O}_4$ sintered at different T_s .

The σ_{ac} can also be explained through the polaron hopping model proposed by Austin and Mott [125]. Variation of $\log\sigma_{ac}$ with $\log\omega$ of the studied compositions sintered at various T_s 1200, 1225 and 1250°C is illustrated in Fig. 4.15. According to the small polaron hopping model (large polaron hopping model) the value of σ_{ac} increases (decreases) with the enhancement of frequency [126]. It is evident from Fig. 4.15 that the mechanism of conduction of the studied samples can be explained by the small polaron hopping model since the value of σ_{ac} increases for all samples with the increase in frequency.

Fig. 4.15 Variation of $\log\sigma_{ac}$ with $\log\omega$ for $Mn_{0.55}Zn_{0.45}Ho_xFe_{2-x}O_4$ sintered at different T_s .

4.8.4 Complex impedance spectra analysis

Complex impedance spectroscopy (CIS) is a very powerful approach for characterizing the electrical properties of materials. Fig. 4.16 illustrates the frequency dependent real part (Z') and imaginary part (Z'') of the impedance for $Mn_{0.55}Zn_{0.45}Ho_xFe_{2-x}O_4$ sintered at various T_s 1200, 1225, and 1250°C. It is evident from Fig. 4.16 (a) that the value of Z' decreases sharply and then remains nearly constant at high frequency region implying the increase in electrical conductivity of the studied compositions. However, at high frequency region the plateau like nature of Z' implies possible occurrence of space charge polarization under the influence of external applied field [127].

Fig. 4.16 Variation of (a) Z' and (b) Z'' with frequency for $\text{Mn}_{0.55}\text{Zn}_{0.45}\text{Ho}_x\text{Fe}_{2-x}\text{O}_4$ sintered at different T_s .

The Z'' exhibits similar nature as Z' [Fig. 4.16 (b)]. The variation of Z'' with frequency exhibits peaks at all compositions. These peaks are observed may be due to the resonance between the applied field frequency and sample frequency. At higher frequency, it also decreases with increasing frequency due to the reduction of loss in the resistive part of the sample. Relaxation peak is appeared indicating the present of immobile charges in $\text{Mn}_{0.55}\text{Zn}_{0.45}\text{Ho}_x\text{Fe}_{2-x}\text{O}_4$.

The complex modulus spectroscopy is a very convenient tool to determine, analyze and interpret the electric transport properties in the materials having the smallest capacitance.

Fig. 4.17 Variation of (a) M' and (b) M'' with frequency for $\text{Mn}_{0.55}\text{Zn}_{0.45}\text{Ho}_x\text{Fe}_{2-x}\text{O}_4$ sintered at different T_s .

The modulus spectra are particularly useful for separating spectral components of the materials having similar resistance but different capacitance. The complex electric modulus is represented by the following expression:

$$\begin{aligned} M^*(\omega) &= J(\omega C_0)Z^* \\ &= M' + jM'' \end{aligned} \quad (5.2)$$

where, $M' = \omega C_0 Z''$ and $M'' = \omega C_0 Z'$, where the symbols have their usual meanings.

Fig. 4.17 (a) shows the frequency dependent real part of electric modulus (M') of $\text{Mn}_{0.55}\text{Zn}_{0.45}\text{Ho}_x\text{Fe}_{2-x}\text{O}_4$ sintered at various T_s 1200, 1225 and 1250°C. At lower frequency the magnitude of M' is nearly zero indicating the ease of polaron hopping [128, 129]. It also implies that the contribution of electrode effect in total impedance is very negligible in case of the studied compositions. However, the magnitude of M' increases gradually with the increase in frequency for all the compositions.

The value of M'' with frequency is shown in Fig. 4.17 (b). It exhibits peaks at the frequency above 10^3 Hz. These peaks indicate the transition from long-range to short range mobility of charge carriers with the increase in frequency. Therefore, charge carriers are mobile in between the grains over the whole frequency range studied in the present case [130]. However, with the increase in frequency the magnitude of M'' is enhanced. Hence, at higher frequency the charge carriers may be trapped in a potential well and are allowed to mobile over short distances (inside the grains) [130]. The dielectric properties of materials would arise due to contributions from intra-grain, inter-grain and electrode processes [131]. The intra-grain and inter-grain processes depend upon the constituents and the processing parameters. Therefore, to understand the effect of additives and the processing parameters, the intra-grain (i.e. grain, g), inter-grain (i.e. grain-boundary, g_b) and electrode contributions have to be separated. The method of complex impedance analysis has emerged as a very powerful tool for this. In this method, the imaginary part, Z'' , of the experimentally measured impedance: $Z^* = Z' - jZ''$ of the material, is plotted as a function of real part, Z' , over a range of frequencies. If the contributions from all the three sources mentioned above (intra-grain, inter-grain and electrode) have single but different of relaxation time, then three semi-circular arcs with their centers on the Z' axes are obtained. The arc with highest frequency range passing through the origin represents the grains effect; the one with the intermediate frequency range gives the contributions

dielectric contribution comes from both the grain and grain boundary resistance at high frequency.

Fig. 4.18 (b) shows the equivalent circuit consists of three parallel RC circuits (R_g/C_g and R_{gb}/C_{gb}) connected in series. In a Nyquist plot (Z'' vs Z' plot) each RC component of the equivalent circuit generates a semicircle. Formation of a single semicircle indicates only the grain effects in the total resistance. Similarly, the formation of second and third semicircular arc corresponds to the grain boundary and electrode effects respectively.

5. CONCLUSIONS

5.1 Conclusions

The $\text{Mn}_{0.55}\text{Zn}_{0.45}\text{Ho}_x\text{Fe}_{2-x}\text{O}_4$ ($x = 0.00, 0.03, 0.06, 0.09, \text{ and } 0.12$) have been synthesized and studied the structural, magnetic and electrical properties. The following conclusions have been drawn from the study of $\text{Mn}_{0.55}\text{Zn}_{0.45}\text{Ho}_x\text{Fe}_{2-x}\text{O}_4$.

- The XRD analysis of various $\text{Mn}_{0.55}\text{Zn}_{0.45}\text{Ho}_x\text{Fe}_{2-x}\text{O}_4$ confirms that samples with small amount of Ho^{3+} content have fairly single phase cubic spinel structure.
- The lattice constant slightly increases with increasing of Ho^{3+} content in $\text{Mn}_{0.55}\text{Zn}_{0.45}\text{Ho}_x\text{Fe}_{2-x}\text{O}_4$.
- The value of ρ_x was found to be higher than that of ρ_B . P with Ho^{3+} content followed the opposite trend of ρ_B .
- P of the samples increases with increasing Ho^{3+} contents. At higher sintering temperatures density decreases, because the intragranular porosity increases as a result of discontinuous grain growth that leads to decrease the sintered density.
- Average grain size is increased up to $x=0.03$, and then decreased with further increasing Ho^{3+} content. These because of increment in Ho^{3+} content into $\text{Mn}_{0.55}\text{Zn}_{0.45}\text{Ho}_x\text{Fe}_{2-x}\text{O}_4$ which may lead to increase in the internal stress, resulting smaller grain size.
- The value of μ_i' is increased up to $x=0.03$ for all T_s , and then decreased with further increasing Ho^{3+} content. The maximum μ_i' of ~ 338 is observed for sample $x=0.03$ sintered at 1225°C . No f_r is observed for $x=0.09$ and $x=0.12$ samples because f_r range is above the studied frequency range.
- It is observed that $\tan\delta_M$ decreases with increasing frequency. The highest value of RQF is observed about (6652) for $x=0.03$. RQF is found to decrease with further increasing Ho^{3+} content because of abnormal grain growth occurs, which creates trapped pores inside the grain.

- The values of M_s are found to be decreased with increasing Ho^{3+} content for all the samples. The content of Fe^{3+} at ferrite lattice sites was decreased resulting to the decrease in magnetization due to the substitution of Ho^{3+} .
- For increasing Ho^{3+} content ϵ' decreases, however it becomes frequency independent with larger bandwidth. This phenomenon can be explained by the Koops theory based on Maxwell–Wagner model.
- The values of σ_{ac} at lower frequency is found almost constant whereas after a certain frequency ($>10^4$ Hz) σ_{ac} increases very fast.
- The value of Z' decreases with increasing frequency indicates the increase of conductivity in the composition. On the other hand, Z'' decreases due to the reduction of loss in the resistive part of the sample and relaxation occurs due to the presence of immobile charges.
- The transition frequency of long range to short range mobility of charge carrier increases with increasing the sintering temperature.
- The Cole-Cole plot of $\text{Mn}_{0.55}\text{Zn}_{0.45}\text{Ho}_x\text{Fe}_{2-x}\text{O}_4$ indicates that, dielectric contribution of some samples come from both the grain and grain boundary effect.

5.2 Suggestions for Future Work

Following recommendations are made for further extension of the present work:

- Mössbauer spectroscopy can be performed to know the cation distribution.
- Magnetoelectric coefficient can be performed to know the multiferroic behavior of the studied samples.
- Ferroelectric (P-E) hysteresis loop measurement can be performed to know the ferroelectric nature of the studied compositions
- Investigation of temperature dependent electromagnetic properties.

Novelty of the Present Research

Ho³⁺ substitution (3%) has significantly improved the initial permeability (about double, 170 to 330) compared to that of the parent composition.

References

- [1] Konig, U., "Substitutions in manganese zinc ferrites", *Applied Physics*, Vol. 4, pp. 237-242, 1974.
- [2] Gadkari, A. B., Shinde, T. J., Vasambekar, P.N., "Structural analysis of Y³⁺ doped Mg–Cd ferrites prepared by oxalate co-precipitation method", *Materials Chemistry and Physics*, Vol. 114, pp. 505-510, 2009.
- [3] Rezlescu, E., Sachelarie L., Popa P. D., and Rezlescu, N., "Effect of substitution of divalent ions on the electrical and magnetic properties of Ni-Zn-Me ferrites", *IEEE Transactions on Magnetism*, Vol. 36, pp. 3962-3967, 2000.
- [4] Bharathi, K.K., Chelvane J.A., Markandeyulu, G., "Magnetoelectric properties of Gd and Nd-doped nickel ferrite", *J. Magn. Magn. Mater.*, Vol. 321, pp. 3677-3680, 2009.
- [5] Peng J., Hojamberdiev, M., Xu, Y., Cao, B., wang, J., Wu, H., "Hydrothermal synthesis and magnetic properties of gadolinium-doped CoFe₂O₄ nanoparticles", *J. Magn. Magn. Mater.*, Vol. 323, pp. 133-137, 2011.
- [6] Guo, L., Meng, X., Feng, Y., "Effect of Sm³⁺ ions doping on structure and magnetic properties of nanocrystalline NiFe₂O₄ ferrites", *J. Alloys Compd.*, Vol. 490, pp. 301-306, 2010.
- [7] Nikumbh, A.K., Pawar, R.A., Nighot, D.V., Gugale, G.S., Sangale, M.D., Khanvilkar, M.B., Negawade, A.V., "Structural, electrical, magnetic and dielectric properties of rare-earth substituted cobalt ferrites nanoparticles synthesized by the co-precipitation method", *J. Magn. Magn. Mater.*, Vol. 355, pp. 201-209, 2014.
- [8] Gama, L., Diniz, A. P., Costa, A. C. F. M., Bezende, S. M., Azevedo, A., and Cornejo, D. R., "Magnetic properties of nanocrystalline Ni-Zn ferrites doped with samarium", *Physica B: Condens. Matter.*, Vol. 384, pp. 97-99, 2006.
- [9] Jcoba, S. E., Dukalde, S., Bertorella, H. R., "Rare earth influence on the structural and magnetic properties of NiZn ferrites", *J. Magn. Magn. Mater.*, Vol. 272, pp. 2253-2254, 2004.

- [10] Syue, M. R., Wei, F. J., Chou, C. S., Fu, C. M., “Magnetic and electrical properties of Mn–Zn ferrites synthesized by combustion method without subsequent heat treatments”, *J. Appl. Phys.*, Vol. 109, pp. 320-324, 2011.
- [11] Ai, L., Jiang, J., “Influence of annealing temperature on the formation, microstructure and magnetic properties of spinel nanocrystalline cobalt ferrites”, *Current Appl. Phys.*, Vol. 10, pp. 284–288, 2010.
- [12] Juliana, B S., Walter, D. B., Nelcy, D.S., “Influence of heat treatment on cobalt ferrite ceramics powders”, *Materials Science and Engineering*, Vol. B112, pp. 182-187, 2004.
- [13] Irfan, S., Ajaz-un-Nabi, M., Jamil, Y., Amin, N., “Synthesis of $Mn_{1-x}Zn_xFe_2O_4$ ferrite powder by co-precipitation method”, *Mater Sci Eng.*, Vol. 60(1), pp. 012048, 2014.
- [14] Saleem, M. and Varshney, D., “Influence of transition metal Cr^{2+} doping on structural, electrical and optical properties of Mn-Zn aluminates”, *J. Alloys Compd.*, Vol. 708, pp. 397-403, 2017.
- [15] Thakur, P., Sharma, R., Sharma, V., Barman, P.B., Kumar, M., Barman, D., Katyal, S.C., Sharma, P., “ Gd^{3+} doped Mn-Zn soft ferrite nanoperticles: Superparamagnetism and its correlation with other physical properties”, *J. Magn. Magn. Mater.*, Vol. 432 pp. 208-217, 2017.
- [16] Ravinder, D. and Ravi Kumar, B., “A study on elastic behaviour of rare earth substituted Mn-Zn ferrites”, *Materials Letters*, Vol. 57, pp. 4471-4473, 2003.
- [17] Jagadeesha Angadi, V., Rudraswamy, B., Sadhana, K., Ramana Murthy, S. and Praveena, K., “Effects of Sm^{3+} & Gd^{3+} on structural, electrical and magnetic properties of Mn-Zn ferrites synthesized via combustion route”, *J. Alloys Compd.*, Vol. 656, pp. 5-12, 2016.
- [18] Sugimoto M., “The past, present, and future of ferrites”, *J. Am. Ceram. Soc.*, Vol. 82, pp. 269–280, 2004.
- [19] Skołoszewska, B., Tokarz, W., Przybylski, K., Kakol, Z., “Preparation and magnetic properties of MgZn and MnZn ferrites”, *Physica C: Superconductivity and Its Applications.*, Vol. 387, pp. 290–294, 2003.
- [20] Henderson, C. M. B., Charnock, J.M., Plant, D. A., “Cation occupancies in Mg, Co, Ni, Zn, Al ferrite spinels: a multi-element EXAFS study”, *J. Phys. Condens. Matter*, Vol. 19 (076214) pp. 1-25, 2007.

- [21] Tatarchuk, T. R., Bououdina, M., Paliychuk, N. D., Yaremiy, I. P., Moklyak, V. V., “Structural characterization and antistructure modeling of cobalt-substituted zinc ferrites”, *J. Alloys Compd.* Vol. 694, pp. 777–791, 2017.
- [22] Namai, A., Yoshikiyo, M., Yamada, K., Sakurai, S., Goto, T., Yoshida, T., Miyazaki, T., Nakajima, M., “Hard magnetic ferrite with a gigantic coercivity and high frequency millimetre wave rotation”, *Nat. Commun.* Vol. 3, pp. 1035–1036, 2012.
- [23] Martirosyan, K.S., Martirosyan, N. S., Chalykh, A. E., “Structure and properties of hard-magnetic barium, strontium, and lead ferrites”, *Inorganic Materials*, Vol. 39, pp. 866–870, 2003.
- [24] Costa, A. C. F. M., Diniz, A. P. A., De Melo, A. G. B., Kiminami, R. H. G. A., Cornejo, D. R., Costa, A. A., Gama, L., “Ni-Zn-Sm nanopowder ferrites: morphological aspects and magnetic properties”, *J. Magn. Magn Mater.* Vol. 320 pp. 742–749, 2008.
- [25] Mansour, S. F., Hemeda, O. M., Abdo, M. A., Nada, W. A., “Improvement on the magnetic and dielectric behavior of hard/soft ferrite nanocomposites”, *J. Mol. Struct.* Vol. 1152, pp. 207–214, 2018.
- [26] Sun, T., Borrasso, A., Liu, B., Dravid, V., “Synthesis and characterization of nanocrystalline zinc manganese ferrite”, *J. Am. Ceram. Soc.*, Vol. 94, pp. 1490–1495, 2011.
- [27] Kirchmayr, H. R., “Permanent magnets and hard magnetic materials”, *J. Appl. Phys.*, Vol. 29, pp. 2763–2778, 1996.
- [28] Torkian, S., Ghasemi, A., Razavi, R. S., “Magnetic properties of hard-soft $\text{SrFe}_{10}\text{Al}_2\text{O}_{19}/\text{Co}_{0.8}\text{Ni}_{0.2}\text{Fe}_2\text{O}_4$ ferrite synthesized by one-pot sol-gel autocombustion”, *J. Magn. Magn Mater.*, Vol. 416, pp. 408–416, 2016.
- [29] Chin, T. S., “Permanent magnet films for applications in microelectromechanical systems”, *J. Magn. Magn Mater.*, Vol. 209, pp. 75–79, 2000.
- [30] Ji, H., Lan, Z., Yu Z., Zhiyong X., “Microstructure and temperature dependence of magnetic properties of MnZnTiSn ferrites for power applications”, *IEEE Trans. Magn.* Vol. 46, pp. 974–978, 2009.
- [31] Herrera, G., “Domain wall dispersions: relaxation and resonance in Ni-Zn ferrite doped with V_2O_3 ”, *J. Appl. Phys.*, Vol. 108, pp. 3–8, 2010.

- [32] Fűzer, J., M. Strečková, M., Dobák, S., Ďáková, P., Kollár, M., “Innovative ferrite nanofibres reinforced soft magnetic composite with enhanced electrical resistivity”, *J. Alloys Compd.*, Vol. 753, pp. 219–227, 2018.
- [33] Zhao, H., Ragusa, C., Appino, C., De La Barriere, O., Wang, Y., Fiorillo, F., “Energy losses in soft magnetic materials under symmetric and asymmetric induction waveforms”, *IEEE Trans. Power Electron.*, Vol. 34, pp. 2655–2665, 2019.
- [34] Justin Joseyphus, R., Narayanasamy, A., Shinoda, K., Jeyadevan, B., Tohji, K., “Synthesis and magnetic properties of the size-controlled Mn-Zn ferrite nanoparticles by oxidation method”, *J. Phys. Chem. Solid.*, Vol. 67, pp. 1510–1517, 2006.
- [35] Miclea, C., Tanasoiu, C., Miclea, C. F., Gheorghiu, A., Tanasoiu, V., “Soft ferrite materials for magnetic temperature transducers and applications”, *J. Magn. Magn Mater.*, Vol. 290, pp. 1506–1509, 2005.
- [36] Son, S., Swaminathan, R., McHenry, M. E., “Structure and magnetic properties of rf thermally plasma synthesized Mn and Mn-Zn ferrite nanoparticles”, *J. Appl. Phys.*, Vol. 93, pp. 7495–7497, 2003.
- [37] Tűpfer, J., Műrbe, J., Angermann, A., Kracunovska, S., Barth, S., Bechtold, F., “Soft ferrite materials for multilayer inductors”, *Int. J. Appl. Ceram. Technol.*, Vol. 3, pp. 455–462, 2006.
- [38] Razzitte, A. C., Jacobo, S. E., Fano, W. G., “Magnetic properties of MnZn ferrites prepared by soft chemical routes”, *J. Appl. Phys.*, Vol. 87, pp. 6232–6234, 2002.
- [39] Li, M., Fang, H., Li, H., Zhao, Y., Li, T., Pang, H., Tang, J., Liu, X., “Synthesis and characterization of MnZn ferrite nanoparticles with improved saturation magnetization”, *J. Supercond. Nov. Magnetism.*, Vol. 30, pp. 2275–2281, 2017.
- [40] Fujita, A., Gotoh, S., “Temperature dependence of core loss in Co-substituted MnZn ferrites”, *J. Appl. Phys.* Vol. 93, pp. 7477–7479, 2003.
- [41] Baguley, C. A., Madawala, U.K., Carsten, B., “The influence of remanence on magnetostrictive vibration and hysteresis in Mn-Zn ferrite cores”, *IEEE Trans. Magn.*, Vol. 48, pp. 1844–1850, 2012.

- [42] Ying, Y., Gong, Y., Liu, D., Li, W., Yu, J., “Effect of MoO₃ addition on the magnetic properties and complex impedance of Mn–Zn ferrites with high bsand high initial permeability”, *J. Supercond. Nov. Magnetism.*, Vol. 30, pp.2129–2134, 2017.
- [43] Verma, A., Alam, M. I., Chatterjee, R., “Development of a new soft ferrite core for power applications”, *J. Magn. Magn Mater.*, Vol. 300, pp. 500–505, 2006.
- [44] Tsakaloudi, V., Zaspalis, V., “Synthesis of a low loss Mn-Zn ferrite for power applications”, *J. Magn. Magn Mater.*, Vol. 400, pp. 307–310, 2016.
- [45] Patel, J., Parekh, K., Upadhyay, R. V., “Performance of Mn-Zn ferrite magnetic fluid in a prototype distribution transformer under varying loading conditions”, *Int. J. Therm. Sci.* Vol. 114, pp. 64–71, 2017.
- [46] Latorre-Esteves, M., Cortés, A., Torres-Lugo, M., Rinaldi, C., “Synthesis and characterization of carboxymethyl dextran-coated Mn/Zn ferrite for biomedical applications”, *J. Magn. Magn Mater.*, Vol. 321, pp. 3061–3066, 2009.
- [47] Zhao, L. J., Cui, Y. M., Yang, H., Yu, L. X., Jin, W. Q., Feng, S. H., “The magnetic properties of Ni_{0.7}Mn_{0.3}Gd_xF_{2-x}O₄ ferrite”, *Mater. Lett.*, Vol- 60, pp 104-108, 2006.
- [48] Rezlescu, N., et al., “Effects of the rare-earth ions on some properties of a nickel-zinc ferrite”, *J. Phys.: Condens. Matter*, Vol. 6 (29) pp. 5707, 1994.
- [49] Ahmed, M. A., Okasha, N., El-Sayed, M. M., “Enhancement of the physical properties of rare-earth-substituted Mn–Zn ferrites prepared by flash method”, *Ceramics International.*, Vol-33, pp 49-58, 2007.
- [50] Peng, Z., Fu, X., Ge, H., Fu, Z., Wang, C., Qi, L., Miao, H., “Effect of Pr³⁺ doping on magnetic and dielectric properties of Ni–Zn ferrites by one-step synthesis”, *J. Magn. Magn. Mater.*, Vol. 323, pp. 2513–2518, 2011.
- [51] Feng, X., Xiangchun, Z., Liangchao, L., Hui, L., Jiang, J., “Synthesis, magnetic properties and microstructure of Ni–Zn–Cr ferrites doped with lanthanum”, *Journal of Rare Earths.*, Vol. 25 pp. 232-236, 2007.
- [52] Al Angari, Y. M., “Magnetic properties of La-substituted NiFe₂O₄ via egg-white precursor route, *J. Magn. Magn. Mater.*, Vol. 323, pp. 1835–1839, 2011.

- [53] Ishaque, M., Islama, M. U., Khan, M. A., Rahman, I. Z., Genson, A., Hampshire, S., “Structural, electrical and dielectric properties of yttrium substituted nickel ferrites”, *Physica B.*, Vol. 405 (6), pp.1532–1540, 2010.
- [54] Bloeman, M., Vandendriessche, S., Goovaerts, V., Brullo, W., Vanbe, M., Carron, S., Geukens, N., Parac-Vogt, T., Verbiest, T., “Synthesis and characterization of Holmium-doped iron-oxide nanoparticles”, *Materials Letters*, Vol. 7, pp. 1155-1164. 2014.
- [55] Murtaza Rai, G., Iqbal, M. A., Kubra, K. T., “Effect of Ho^{3+} substitutions on the structural and magnetic properties of $\text{BaFe}_{12}\text{O}_{19}$ hexa ferrites”, *J. Alloys Compd.*, Vol. 495, pp. 229–233, 2010.
- [56] Patankar, K.K., Ghone, D.M., Mathe, V.L., Kaushik, S.D., “Structural and physical property study of Sol-gel synthesized $\text{CoFe}_2\text{-XHoxO}_4$ nono ferrites”, *J. Magn. Magn. Mater.*, Vol. 454, pp. 71-77. 2018.
- [57] Karimunnesa, S., Atique Ullah, A.K.M., Hasan, M.R., Shanta, F.S., Islam, R., Khan, M.N.I., “Effect of Holmium substitution on the structural, Magnetic and transport properties of $\text{CoFe}_2\text{-XHoxO}_4$ ferrites”, *J. Magn. Magn. Mater.*, Vol. 457, pp. 57-63, 2018.
- [58] Ali, I., Islam, M. U., Ishaque, M., Khan, H. M., Muhammad, N. A., Rana, M. U., “Structural and magnetic properties of holmium substituted cobalt ferrites synthesized by chemical co-precipitation method”, *J. Magn. Magn. Mater.*, Vol. 324, pp. 3773–3777, 2012.
- [59] Angadi Jagdeesha, V., Choudhury, L., Sadhana, K., Lin Liu, H., Matteppanavar, S., Rudraswamy, B., Anavekar, R. V., “Structural, electrical and magnetic properties of Sc^{3+} doped Mn-Zn ferrite nanoparticles”, *J. Magn. Magn. Mater.*, Vol. 424, pp 1-11, 2017.
- [60] D’souza, A., Kumar, D. M., Chatim, M., Naik, V., Naik, P., Tangsali, R. B., “Effect of rare-earth doping on magnetic and electrical transport properties of nanoparticle Mn-Zn ferrite”, *Advanced Science Letters*, Vol. 22(4), pp 773-779, 2016.
- [61] Jagadeesha, A. V., Rudraswamy, B., Sadhana, K., Murthy, R. S., Praveena, K., “Effect of Sm^{3+} - Gd^{3+} on structural, electrical and magnetic properties of Mn-Zn ferrites synthesized via combustion route”, *J. Alloys Compd*, Vol. 656, pp. 5-12, 2016.

- [62] Alina, M., Muhammad, A. K., Muhammad, Y. K., Majid, N. K., “Tuning magnetic and high frequency dielectric behavior in Ni-Zn ferrites by Ho doping”, *Ceramics International.*, Vol. 44, pp. 6321-6329, 2018.
- [63] Lohar, K. S., Pachpinde, A. M., Kadam. R. H., “Self-propagating high temperature synthesis, structural morphology and magnetic interactions in rare earth Ho³⁺ doped CoFe₂O₄ nanoparticles”, *J. Alloys Compd.*, Vol. 604, pp. 204-210, 2014.
- [64] Ghafoor, A., khan, A. M., Islam, I. U., Gilani, A. Z., Manzoor, A., Ali, I., and Warsi, M. F., “Structural and electromagnetic studies of Ni_{0.7}Zn_{0.3} Ho_{2x}Fe_{2-2x}O₄ ferrites”, *Ceramics International*, Vol. 42, pp. 14252-14256, 2016.
- [65] Erum, P., Gul, I. H., “High frequency AC response, DC resistivity and magnetic studies of holmium substituted Ni-ferrite: A novel electromagnetic material”, *J. Magn. Magn. Mater.*, Vol. 349, pp. 27-34, 2014.
- [66] Alina, M., Muhammad, A. K., Muhammad, S., Muhammad, F. W., “Investigation of structural, dielectric and magnetic properties of Ho substituted nanostructured lithium ferrites synthesized via auto-citric combustion route”, *J. Alloys Compd.*, Vol. 710, pp. 547-556, 2017.
- [67] Valenzuela, R., *Magnetic Ceramics*, Cambridge University Press, Cambridge, 1994.
- [68] Goldman, A., *Handbook of Modern Ferromagnetic Materials*, Kulwer Acad. Pub, Boston, U.S.A, 1999.
- [69] Shah, M. R., Dielectric properties of alkaline earth (D = Ba, Sr, Ca) and rare earth (T = La, Nd) substituted polycrystalline D_{1-x}T_x(Ti_{0.5}Fe_{0.5})O₃ perovskite, Ph. D. Thesis, Department of Physics, Bangladesh University of Engineering and Technology, 2013.
- [70] West, A.R., *Solid state chemistry and its applications*. John Wiley & Sons, 2014.
- [71] Gerand, B., Nowogrocki, G., Guenot, J. and Figlarz, M. *Preparative methods in Solid State Chemistry*. Academic press, 1989.
- [72] Moulson, A. J. and Herbert, J. M., *Electroceramics: Materials, Properties, Applications*. Chapman & Hall, U.K 1990.
- [73] Xu, Y., *Ferroelectric Materials and Their Applications*. Elsevier Science Pub. Co. New York, USA, 1991.

- [74] “Calcination.” Wikipedia, Wikimedia Foundation, en.wikipedia.org/wiki/Calcination, 18 Nov. 2018.
- [75] Peláiz-Barranco, A. and Guerra, J.D.L.S., “Dielectric relaxation phenomenon in ferroelectric perovskite-related structures”, In *Ferroelectrics*. InTech., 2010.
- [76] Coble, R. L. and Burke, J. E., “On the reactivity of solids”, 4th Int. Symp., 30 May-4 June, Amsterdam, pp. 38-51, 1960.
- [77] Miah, M. J., “Study of Multiferroic Properties of Rare Earth Substituted $x\text{Ba}_{0.95}\text{Sr}_{0.05}\text{TiO}_3+(1-x)\text{BiFe}_{0.9}\text{Re}_{0.1}\text{O}_3$ Perovskite Ceramics”, Ph. D. Thesis, Department of Physics, Bangladesh.
- [78] Huang, D., Liu, Z., Li, Y., and Liu, Y., “Colossal permittivity and dielectric relaxation of (Li, In) Co-doped ZnO ceramics,” *J. Alloy. Compd.*, vol. 698, pp. 200-206, 2017.
- [79] Kittel, C.; *Introduction to Solid State Physics*, 7th edition, Jhon Wiley & Sons, Inc., Singapore 1996.
- [80] Bragg, W. H., “The structure of magnetite and the spinets”, *Nature*, Vol-95, pp 561, 1915.
- [81] Gadkari, A. B.; Shinde, T. J.; Vasambekar, P. N.; “Structural and magnetic properties of nanocrystalline Mg-Cd ferrites prepared by oxalate coprecipitation method,” *J. Mater Sci: Mater Electron*, Vol. 21(1), pp 96-103, 2010.
- [82] Hossain, A. K. M. Akther., “Investigation of colossal magnetoresistance in bulk and thick film magnetites,” Ph. D. Thesis, Imperial College, London, 1998.
- [83] Buchanan, R. C., “Ceramic Materials for Electronics”, Marcel Dekker, Inc, New York, 2004.
- [84] Jaffe, B., Cook, W. R., and Jaffe, H., “Piezoelectric Ceramics”, Academic Press, London, 1971.
- [85] Mendelson, M. I., “Average grain size in polycrystalline ceramics,” *J. Am. Ceram. Soc.*, vol. 52 (8), pp. 443-446, 1969.
- [86] Cole, K. S., and Cole, R. H., “Dispersion and Absorption in Dielectrics I. Alternating. Current Characteristics”, *J. Chem. Phys.*, Vol. 9, pp. 341-351, 1941.

- [87] Goldman, A., “Handbook of modern ferromagnetic materials”, Springer Science & Business Media, Vol. 505, 2012.
- [88] Hossen, M. B., Study of physical, magnetic and transport properties of cations substituted NiCuZn based spinel ferrites, Ph. D. Thesis, Department of Physics, Bangladesh University of Engineering and Technology, 2015.
- [89] Barsoukov, E. and Macdonald, J. R., “Impedance Spectroscopy Theory, Experiments and Applications”, 2nd edition (Hoboken, NJ: Wiley), pp. 34-46, 2005.
- [90] Macdonald, J. R., “Impedance Spectroscopy”, Wiley, New York, 1987.
- [91] Rahman, M.A. and Hossain, A. K. M. Akther, “Relaxation mechanism of (x) $Mn_{0.45}Ni_{0.05}Zn_{0.50}Fe_2O_4+(1-x)BaZr_{0.52}Ti_{0.48}O_3$ multiferroic materials,” *Physica scripta.*, vol. 89 (11), pp. 115811, 2014.
- [92] Rafique, M., Study of the Magnetoelectric Properties of Multiferroic Thin Films and Composites for Device Applications, Ph. D. Thesis, Department of Physics, COMSATS Institute of Information Technology, 2014.
- [93] Momin, A.A., Parvin, R. and Hossain, A. K. M. Akther, “Structural, morphological and magnetic properties variation of nickel-manganese ferrites with lithium substitution,” *J. Magn. Magn. Mater.*, vol. 423, pp. 124-132, 2017.
- [94] Ataa, A. M. A., El, Attiab, S. M., Konya, D. El, and Al-Hammadic, A. H., “Spectral, initial magnetic permeability and transport studies of $Li_{0.5-0.5x}Co_xFe_{2.5-0.5x}O_4$ spinel ferrite”, *J. Magn. Magn. Mater.*, Vol - 295, No. 1, pp 28-36, 2005.
- [95] Guo, L., Xiangqian, S., Xianfeng, M., Yuhua, F., “Effect of Sm ions doping on structure and magnetic properties of nanocrystalline $NiFe_2O_4$ fibers”, *J. Alloy. Compd.*, Vol-490, pp 301–306, 2010.
- [96] Jacob, B.P., Thankachan, S., Xavier, S., Mohammed, E.M., “Effect of Gd doping on the structural and magnetic properties of nanocrystalline Ni–Cd mixed ferrite”, *Physica Scripta.*, Vol-84 , 045702, 2011.
- [97] Lohar, K. S., Pachpinde, A. M., Langade, M. M., Kadam, R. H., Shirsath, S. E., “Self-propagating high temperature synthesis, structural morphology and magnetic interactions in rare earth Ho^{3+} doped $CoFe_2O_4$ nanoparticles”, *J. Alloys. Compd.*, Vol- 604, pp 204-210, 2014.

- [98] Coble, R. L. and Burke, J. E., "On the reactivity of solids", 4th Int. Symp., 30 May-4 June, Amsterdam, pp. 38-51, 1960.
- [99] Costa, A. C. F. M., Tortella, E., Morelli, M. R., and Kiminami, R. H. G. A., "Synthesis, microstructure and magnetic properties of Ni-Zn ferrites," *J. Magn. Magn. Mater.*, 256, 174, 2003.
- [100] Globus, A. and Duplex, P., "Separation of susceptibility mechanisms for ferrites of low anisotropy," *IEEE Trans. Magn.*, vol. 2(3), pp. 441-445, 1966.
- [101] Ishaque, M., Islam, M.U., Rahman, I. Z. "Structural, electrical and dielectric properties of yttrium substituted nickel ferrites", *Physica B*, Vol- 405 pp 1532–1540, 2010.
- [102] Snoek, J. L., "Dispersion and absorptions in magnetic ferrites at frequencies above Mc/s", *Physica B*, Vol- 14, pp 207-217, 1948.
- [103] Yu, M., Hu, J., Liu, J. and Li, S., "Electromagnetic properties of multiferroic magnetoelectric BaTiO₃-Co_xFe_{3x}O₄ core-shell particles obtained by homogeneous co-precipitation," *J. Magn. Magn. Mater.*, vol. 326, pp. 31-34, 2013.
- [104] Kumar, P., Sharma, S.K., Knobel, M. and Singh, M., "Effect of La³⁺ doping on the electric, dielectric and magnetic properties of cobalt ferrite processed by co-precipitation technique," *J Alloys Compd.*, vol. 508(1), pp. 115-118, 2010.
- [105] Verma, A. and Chatterjee, R., "Effect of zinc concentration on the structural, electrical and magnetic properties of mixed Mn-Zn and Ni-Zn ferrites synthesized by the citrate precursor technique," *J. Magn. Magn. Mater.*, vol. 306(2), pp. 313-320, 2006..
- [106] Jun, H. and Mi, Y., "Preparation of high permeability Ni-Cu-Zn ferrite", *J. Zhejiang. Uni. Sci.*, Vol - 6B No. 6, pp 580-583, 2005.
- [107] Tsutaoka, T., Ueshima, M., Tokunaga, T., Nakamura T. and Hatakeyama, K., "Frequency dispersion and temperature variation of complex permeability of Ni-Zn ferrite composite materials", *J. Appl. Phys.*, Vol - 78, No. 6, pp 3983, 1995.
- [108] Hu, J. and Yan, M., "Preparation of high-permeability NiCuZn ferrite", *J. Zhejiang. Uni. Sci.*, Vol-6, No. 6, pp 580-583, 2005.

- [109] Brailsford, F., *Physical Principles of Magnetism*, D. Van Nostrand Company Ltd., London, 1966.
- [110] Cullity, B. D., “Introduction to Magnetic Materials”, Addison-Wesley Publishing Company, Inc., California 1972.
- [111] Rado, G.T., Wright, R.W., Emerson, W. H. and Terris, A., “Ferromagnetism at Very High Frequencies. IV. Temperature Dependence of the Magnetic Spectrum of a Ferrite”, *Phys. Rev.*, Vol-88, pp 909-915, 1952.
- [112] Gama, A. M. and Rezende, M. C., “Complex permeability and permittivity variation of radar absorbing materials based on MnZn ferrite in microwave frequencies”, *Mat. Res.*, Vol. 16, pp. 997-1001, 2013.
- [113] Rashad, M. M., Mohamad, R. M., El-Shall, H., “Magnetic properties of Nanocrystalline Sm- substituted CoFe_2O_4 synthesized by citrate precursor method”, *J. Mater. Process. Technol.*, Vol-198, pp 139-146, 2008.
- [114] Koops, C.G., “On the dispersion of resistivity and dielectric constant of some semiconductors at audio frequencies,” *Phys. Rev.*, vol. 83(1), pp. 121, 1951.
- [115] Maxwell, J. C. (1973) *Electricity and Magnetism*, Oxford University Press, London.
- [116] Wagner, K.W., “Zur theorie der unvollkommenen dielektrika,” *Ann. Phys.*, vol. 345(5), pp. 817-855, 1913.
- [117] Verma, A., Thakur, O. P, Prakash, C., Goel, T.C., and Mendiratta, R.G., “Temperature dependence of electrical properties of nickel–zinc ferrites processed by the citrate precursor technique, *Mater. Sci. Eng.*, Vol. B 116 pp 1–6, 2005.
- [118] Rezlescu, N., and Rezlescu, E., “Dielectric properties of copper containing ferrites”, *Phys. Status Solidi*, Vol. A 23, pp 575–582, 1974.
- [119] Jonker, G. H., “Analysis of the semiconducting properties of cobalt ferrite”, *J. Phys. Chem. Solids*, Vol. 9, pp. 165–175, 1959.
- [120] Jonscher, A. K., “Dielectric Relaxation in Solids”, Chelsea Dielectric Press, London, 1983.
- [121] Lunkenheimer, P., Bobnar, V., Pronin, A. V., Ritus, A. I., Volkov A. A., and Loidhl, A., “Origin of apparent colossal dielectric constants”, *Phys. Rev. B*, Vol-66, 052105; 2002.

- [122] Wagner, K.W., “Zur theorie der unvollkommenen dielektrika,” *Ann. Phys.*, vol. 345(5), pp. 817-855, 1913.
- [123] Miah, M.J., Khan, M.N.I. and Hossain, A. K. M. Akther, “Synthesis and enhancement of multiferroic properties of $(x) \text{Ba}_{0.95}\text{Sr}_{0.05}\text{TiO}_3-(1-x)\text{BiFe}_{0.90}\text{Dy}_{0.10}\text{O}_3$ ceramics,” *J. Magn. Magn. Mater.*, Vol. 397, pp. 39-50, 2016.
- [124] Khandekar, M.S., Kambale, R.C., Patil, J.Y., Kolekar, Y.D. and Suryavanshi, S.S., “Effect of calcination temperature on the structural and electrical properties of cobalt ferrite synthesized by combustion method,” *J. Alloys Compd.*, vol. 509(5), pp.1861-1865, 2011.
- [125] Austin, I.G. and Mott, N.F., “Polarons in crystalline and non-crystalline materials,” *Adv. Phys.*, vol. 18(71), pp. 41-102, 1969.
- [126] Mazumdar, S.C., Khan, M.N.I., Islam, M.F. and Hossain, A. K. M. Akther, “Tuning of magnetoelectric coupling in $(1y)\text{Bi}_{0.8}\text{Dy}_{0.2}\text{FeO}_3-y\text{Ni}_{0.5}\text{Zn}_{0.5}\text{Fe}_2\text{O}_4$ multiferroic composites,” *J. Magn. Magn. Mater.*, vol. 401, pp. 443-454, 2016.
- [127] Kaiser, M., “Electrical conductivity and complex electric modulus of titanium doped nickel–zinc ferrites,” *Physica B*, vol. 407(4), pp. 606-613, 2012.
- [128] Choudhary, R.N.P., Pradhan, D.K., Tirado, C.M., Bonilla, G.E. and Katiyar, R.S., “Effect of La substitution on structural and electrical properties of $\text{Ba}(\text{Fe}_{2/3}\text{W}_{1/3})\text{O}_3$ nanoceramics,” *J. Mater. Sci.*, vol. 42 (17), pp.7423-7432, 2007.
- [129] Pattanayak, S., Choudhary, R.N.P., Das, P.R. and Shannigrahi, S.R., “Effect of Dy-substitution on structural, electrical and magnetic properties of multiferroic BiFeO_3 ceramics,” *Ceram. Int.*, vol. 40(6), pp. 7983-7991, 2014.
- [130] Pandey, L., Katore, R., Parkash, O., and Kumar, D., “Evidence of two ferroelectric PTCR components in valence-compensated ceramic system $\text{Ba}_{1-x}\text{La}_x\text{Ti}_{1-x}\text{Co}_x\text{O}_3$,” *Bul. Mater. Sci.*, 20, pp.933-947, 1997.
- [131] A. K. Jonscher, *Dielectric Relaxation in Solids*, Chelsea Dielectric Press, London, 1983.
- [132] Ye, H., Jackman, R.B. and Hing, P., “Spectroscopic impedance study of nanocrystalline diamond films,” *J. Appl. Phys.*, vol. 94(12), pp. 7878-7882, 2003.

Appendix

List of Presentation

1. **Kundu, N. R.,** Das, M. K., Rahaman, Z., Noman, A. A., and Hossain, A. K. M. Akther, “Investigation of Magnetic and Dielectric Properties of Holmium Substituted Manganese-Zinc Ferrites,” *National Conference On Physics-2019*, organized by Bangladesh Physical Society, 7-9 February 2019, Dhaka University, Dhaka, Bangladesh; Poster No. PP-63.
2. **Kundu, N. R.,** Das, M. K., and Hossain, A. K. M. Akther, “Structural, Magnetic and Dielectric Properties of Ho^{3+} Substituted Mn-Zn Ferrites,” *International Conference On Physics-2020*, organized by Bangladesh Physical Society, 5-7 March 2020, Atomic Energy Centre, Dhaka, Bangladesh; Poster No. PP-31.
3. **Kundu, N. R.,** Das, M. K., and Hossain, A. K. M. Akther, “Role of Holmium in the Structural, Magnetic and Dielectric Properties of Mn-Zn Ferrites,” *6th Conference (Virtual) of Bangladesh Crystallographic Association*, Organized by Bangladesh Crystallographic Association, 15-16 January 2021; Poster No. PP-09 (Zoom Platform).